

Fate of supernova progenitors in massive binary systems

Tomoya Kinugawa⁽¹⁾⁽²⁾⁽³⁾★, Shunsaku Horiuchi⁽⁴⁾⁽⁵⁾†, Tomoya Takiwaki⁽⁶⁾, and Kei Kotake⁽⁷⁾⁽⁸⁾

¹Faculty of Engineering, Shinshu University, 4-17-1, Wakasato, Nagano-shi, Nagano, 380-8553, Japan

²Research Center for Aerospace System, Shinshu University, 4-17-1, Wakasato, Nagano-shi, Nagano, 380-8553, Japan

³Research Center for the Early Universe, Graduate School of Science, University of Tokyo, 7-3-1 Hongo, Bunkyo-ku, Tokyo 113-0033, Japan

⁴Center for Neutrino Physics, Department of Physics, Virginia Tech, Blacksburg, VA 24061, USA

⁵Kavli IPMU (WPI), UTIAS, The University of Tokyo, Kashiwa, Chiba 277-8583, Japan

⁶National Astronomical Observatory of Japan, 2-21-1 Osawa, Mitaka, Tokyo 181-8588, Japan

⁷Research Institute of Stellar Explosive Phenomena, Fukuoka University, 8-19-1 Nanakuma, Jonan-ku, Fukuoka-shi, Fukuoka 814-0180, Japan

⁸Department of Applied Physics, Faculty of Science, Fukuoka University, 8-19-1 Nanakuma, Jonan-ku, Fukuoka-shi, Fukuoka 814-0180, Japan

Accepted XXX. Received YYY; in original form ZZZ

ABSTRACT

How massive stars end their lives depends on the core mass, core angular momentum, and hydrogen envelopes at death. However, these key physical facets of stellar evolution can be severely affected by binary interactions. In turn, the effectiveness of binary interactions itself varies greatly depending on the initial conditions of the binaries, making the situation much more complex. We investigate systematically how binary interactions influence core-collapse progenitors and their fates. Binary evolution simulations are performed to survey the parameter space of supernova progenitors in solar metallicity binary systems and to delineate major evolutionary paths. We first study fixed binary mass ratios ($q = M_2/M_1 = 0.5, 0.7, \text{ and } 0.9$) to elucidate the impacts of initial mass and initial separation on the outcomes, treating separately Type Ibc supernova, Type II supernova, accretion induced collapse (AIC), rapidly rotating supernova (RSN), black hole formation, and gamma ray burst (GRB). We then conduct Binary Population Synthesis calculations for 12 models, varying the initial parameter distributions and binary evolution parameters, to estimate various supernova fractions. We obtain a Milky Way supernova rate $R_{\text{SN}} = (1.14\text{--}1.57) \times 10^{-2} \text{ yr}^{-1}$ which is consistent with observations. We find the rates of AIC, RSN, and GRB to be $\sim 1/100$ the rate of regular supernovae. Our estimated GRB rates are higher than the observed long GRB rate, but very close to the low luminosity GRB rate. Furthering binary modeling and improving the inputs one by one will enable more detailed studies of these and other transients associated with massive stars.

Key words: keyword1 – keyword2 – keyword3

1 INTRODUCTION

Stellar evolution holds paramount importance in astrophysics, providing a foundational framework for not only comprehending the behaviors of stars but also their profound influence on shaping the Universe. By studying how stars form, evolve, and eventually die, one can gain insights into a wide range of astrophysical phenomena, from the properties of individual stars to the formation and evolution of galaxies (Conroy 2013; Nomoto et al. 2013; Smith 2014; Eldridge & Stanway 2022). In particular, supernovae (SNe) and gamma-ray bursts (GRBs) are among the most powerful and intriguing transient phenomenon in the Universe, which are the explosions triggered by the death of massive stars (Woosley et al. 2002; Woosley & Bloom 2006; Smartt 2009; Gehrels et al. 2009).

In a seminal work on stellar evolution, Heger et al. (2003) illustrated that a star’s mass and metallicity determine its eventual fate (see also Woosley et al. 1995, 2002; Woosley & Heger 2007; Sukhbold et al. 2016, for systematic studies). A variety of models are provided

and they are often used in SN modelling (Umeda & Nomoto 2008; Umeda et al. 2012; Sukhbold et al. 2018; Chieffi & Limongi 2020). With the ever-increasing power of supercomputers, studies of the systematic effects of the progenitor mass and metallicity have been explored in multi-dimensional numerical simulations of massive star collapse (Nakamura et al. 2015; Summa et al. 2016; Vartanyan & Burrows 2023; Burrows et al. 2020). Among the many insights they have provided, of particular importance is that the anisotropy of the Si/O shell is enough to alter the course of dynamical evolution of the core-collapse SN (Bollig et al. 2021). Thus, three-dimensional simulations have been performed with limited timescale of the Si/O burning phase to explore more realistic profiles of the progenitors (Couch et al. 2015; Müller et al. 2016b; Mocák et al. 2018; Yoshida et al. 2019, 2021b; Yadav et al. 2020).

One commonly missing ingredient in previous studies of SN progenitors is rotation. This is despite the fact that massive stars initially have high angular momentum (Wolff et al. 2006; Huang et al. 2010) and rotation affects the evolution of stars as strongly as mass and metallicity (e.g., Maeder 2009); for example, centrifugal force, angular momentum transport, and rotation-induced mixing change the stellar structure (see Langer 2012, and the referees therein). Sev-

★ E-mail: kinugawa@shinshu-u.ac.jp

† E-mail: horiuchi@vt.edu

eral evolutionary models have incorporated the impact of rotation (Heger et al. 2000, 2005; Ekström et al. 2012; Georgy et al. 2012). Yoon et al. (2006) have helped to delineate the fate of the massive stars in the parameter space of mass, metallicity and rotation. At the extreme, a star can completely change its evolution when it undergoes chemically homogeneous evolution (CHE) due to efficient mixing induced by rotation (Yoon et al. 2006; Woosley & Heger 2006; Aguilera-Dena et al. 2018). Although CHE may not be common, more generally stars are deformed by rotation; axisymmetric equilibrium structures of rotating stars in two spatial dimensions have been obtained (see Ogata et al. 2023, and the refereces therein). It is imperative to also acknowledge the intricate connection of magnetic fields and rotation in stellar evolution (see Keszthelyi 2023, and refereces therein). A way to handle the shape of the magnetic fields was recently developed (Takahashi & Langer 2021). The effect of rotation and magnetic fields are eagerly studied by three dimensional simulations in the phases right before the core collapse (Varma & Müller 2021; Yoshida et al. 2021a; McNeill & Müller 2022; Fields 2022). The strength of the magnetic field and rotation of stellar cores are thought to even dictate the outcome of explosion, including explosion energies and morphologies, as well as occurrence of SNe versus GRBs (e.g., Iwakami et al. 2014; Summa et al. 2018; Kuroda et al. 2020; Takiwaki et al. 2021; Obergaulinger & Aloy 2022; Varma et al. 2023; Matsumoto et al. 2022; Bugli et al. 2023; Shibagaki et al. 2023; Hsieh et al. 2023).

Therefore, it is not surprising that binary interactions have garnered substantial attention due to their impact on stellar rotation, involving factors such as tidal interactions in binary systems and mass transfer. Moreover, observational evidence suggests a high binary formation rate among high-mass stars (Kobulnicky & Fryer 2007; Mason et al. 2009; Sana et al. 2012, 2013; Chini et al. 2012; Kobulnicky et al. 2014; Moe & Di Stefano 2017). Efforts to incorporate binary effects into stellar evolution codes are ongoing (Cantiello et al. 2007; Patton & Sukhbold 2020; Schneider et al. 2021; Laplace et al. 2021), including even to SN modeling (Vartanyan et al. 2021). The most famous example of a SN from a binary system is perhaps SN1987A (e.g., Menon & Heger 2017; Urushibata et al. 2018; Ono et al. 2020; Utrobin et al. 2021; Nakamura et al. 2022). Observations of the explosion site are still ongoing (Cigan et al. 2019; Larsson et al. 2023). As another example, the SN that created Cassiopeia A may also have been a binary system (Hirai et al. 2020). Also, Betelgeuse may experience a stellar merger (Chatzopoulos et al. 2020). Finally, to make a double neutron star system, an ultra-stripped SN is considered necessary, motivating again binary evolution (Tauris et al. 2017; Yoshida et al. 2017; Müller et al. 2018; Hijikawa et al. 2019).

Nevertheless, while previous studies have explored the contribution of binaries to SNe in specific cases, a systematic understanding akin to the well-established scenario of single stars, as outlined by Heger et al. (2003) and Yoon et al. (2006), remains lacking. To bridge this gap, population synthesis methods emerge as indispensable tools, enabling systematic exploration under a range of assumptions regarding stellar and binary physics, in particular wind mass loss, mass transfer, and common envelope treatments (Hurley et al. 2002; Belczynski et al. 2002; Kinugawa et al. 2014; Zapartas et al. 2017; De Marco & Izzard 2017; Stanway & Eldridge 2018; Spera et al. 2019; Tanikawa et al. 2020; Breivik et al. 2020; Riley et al. 2022; Fragos et al. 2023). The population synthesis method is a numerical calculation technique widely used in binary studies. It is employed to study the evolution and statistical properties of binary stellar systems considering various physics of binary interactions. For example, population synthesis can estimate the gravitational wave sources from

compact binary mergers (e.g., Belczynski et al. 2002; Dominik et al. 2013; Kinugawa et al. 2020) and have predicted the massive stellar-mass binary black hole mergers (Kinugawa et al. 2014, 2016). The impact of the binary evolution on the Diffuse SN Neutrino Background (DSNB) have been studied (Horiuchi et al. 2021). In such studies, the distribution of He or CO core mass is important (Patton et al. 2022; Fragos et al. 2023).

It is in these contexts that we investigate systematically how binary interactions influence SN progenitors. Using simplified models, we focus in particular on the final fates of massive stars: either a “standard” Type II SN, a stripped Ibc SN, a rapidly rotating SN, an accretion induced collapse (AIC), a collapse to black hole, or a GRB. This paper is organized as follows. In Section 2, we describe how to calculate the binary interactions, the stellar evolution, and how to determine the SNe type. Section 3 shows our parameter survey and the binary population synthesis calculations for SNe. In Section 4, we describe the summary of this paper and discussion comparison with previous studies and uncertainties.

2 METHODS

We use the binary population synthesis code in Kinugawa et al. (2014) which is updated from the BSE code (Hurley et al. 2000, 2002) in order to calculate binary evolution effects for SNe. In this section, we describe the main binary effects which change stellar masses and the calculation methods. The other binary interactions are described in Appendix A.

2.1 Stability of mass transfer

If the Roche lobe around a star is fulfilled, the material of the stellar surface is transferred to its companion through the L1 point. The Roche lobe radius of the donor star is approximately described as (Eggleton 1983)

$$R_{L,1} \simeq \frac{0.49q_1^{2/3}}{0.6q_1^{2/3} + \ln(1 + q_1^{1/3})} a, \quad (1)$$

where a , $q_1 = M_1/M_2$, M_1 , and M_2 are the orbital separation, the mass ratio, the mass of the donor, and the mass of the accretor, respectively.

When the mass transfer is dynamically unstable, i.e., the orbit shrink too rapidly that the accretor star will plunge into the envelope of the donor star, the mass transfer become a common envelope phase. On the other hand, when the mass transfer is dynamically stable, the mass transfer continue stably. This case is called the Roche lobe overflow. The dynamical stability of mass transfer is determined by how the stellar radius of the donor star is changed by the mass loss and by how the Roche lobe radius is changed by the mass transfer.

In order to consider the dynamical stability of the mass transfer, we use $\zeta_L = d \log R_{L,1} / d \log M_1$ and $\zeta_{ad} = (d \log R_1 / d \log M_1)_{ad}$. Here, ζ_L is the response of the Roche lobe radius $R_{L,1}$ to the change in the mass of the donor star M_1 and ζ_{ad} is the response of the radius of the donor star R_1 to changes in the mass of the donor star within the dynamical timescale. When $\zeta_L > \zeta_{ad}$, the Roche lobe radius will be much smaller than the stellar radius by the mass transfer in the dynamical timescale. In this case, the mass transfer becomes a common envelope. On the other hand, when $\zeta_L < \zeta_{ad}$, the donor stellar radius will be much smaller than the Roche lobe radius by the mass transfer in the dynamical timescale. In this case, the mass transfer is treated as the Roche lobe overflow. ζ_L is a function of the

mass ratio and the separation of the binary, described as (Eggleton 1983, 2011)

$$\zeta_L = \frac{d \log R_{L,1}}{d \log M_1} \quad (2)$$

$$= \frac{(0.33 + 0.13q_1)[1 + q_1] + (1 - \beta)(q_1^2 - 1) - \beta q_1}{1 + q_1}. \quad (3)$$

On the other hand, ζ_{ad} strongly depends on the evolutionary stage of the donor star. When the donor star is in the red giant phase, ζ_{ad} is described as

$$\zeta_{\text{ad}} = -1 + \frac{2}{3} \frac{M_1}{M_{\text{env},1}}. \quad (4)$$

When the donor star is in other evolutionary phases, ζ_{ad} is 2.59, 6.85, 1.95 and 5.79 for the main sequence phase, the Hertzsprung gap phase (Hjellming 1989), the naked-He main sequence phase and the naked-He giant star (Ivanova et al. 2002; Belczynski et al. 2008), respectively.

2.2 Roche lobe overflow

When the star starts mass transfer ($R_1 > R_{L,1}$) and the mass transfer is dynamically stable ($\zeta_{\text{ad}} > \zeta_L$), the Roche lobe overflow occurs. In order to calculate the mass transfer rate, we use the fitting formula by Hurley et al. (2002),

$$\dot{M}_1 = F(M_1) \left[\ln \left(\frac{R_1}{R_{L,1}} \right) \right]^3 M_\odot \text{ yr}^{-1}, \quad (5)$$

where

$$F(M_1) = 3 \times 10^{-6} \left\{ \min \left[\left(10 \frac{M_1}{10 M_\odot} \right), 5.0 \right] \right\}^2. \quad (6)$$

As the radius of the donor changes by the Kelvin–Helmholtz (KH) timescale, the maximum value of the mass transfer rate from the donor is given by

$$\dot{M}_{1,\text{max}} = \frac{M_1}{\tau_{\text{KH},1}}, \quad (7)$$

where $\tau_{\text{KH},1}$ is the KH timescale of the donor.

The accretion rate to the accretor is described as

$$\dot{M}_2 = -\beta \dot{M}_1. \quad (8)$$

where β is the accretion parameter of the mass transfer. However, if the accretor is a white dwarf, a neutron star or a black hole, we consider the mass accretion rate is limited by the Eddington accretion rate described by

$$\dot{M}_{\text{Edd}} = -\frac{4\pi c R_2}{\kappa_T} = 2.08 \times 10^{-3} (1 + X)^{-1} \left(\frac{R_2}{R_\odot} \right) M_\odot \text{ yr}^{-1}, \quad (9)$$

where R_2 , $\kappa_T = 0.2(1 + X) \text{ cm}^2 \text{ g}^{-1}$, and $X = 0.76$ are the stellar radius of the accretor, the Thomson scattering opacity, and the hydrogen mass fraction, respectively.

We calculate the spin angular momentum evolution of stars in a binary system during the RLOF. The spin angular momentum is carried from the donor to the accretor. We estimate the spin angular momentum loss of the donor in this process with a thin shell approximation:

$$\frac{dJ_{\text{sp},1}}{dt} = \frac{2}{3} \dot{M}_1 R_1^2 \Omega_{\text{spin},1}, \quad (10)$$

where $\Omega_{\text{spin},1}$ is the spin angular velocity of the donor. For the spin angular momentum of the accretor, we consider whether the

transferred mass accretes via an accretion disk or not. First, if there is no accretion disk, i.e., the secondary radius is larger than the critical radius described by

$$r_{\text{cri}} = 0.07225a(q_2(1 + q_2))^{1/4}, \quad (11)$$

where $q_2 = M_2/M_1$ (Lubow & Shu 1975; Ulrich & Burger 1976; Hurley et al. 2002), we assume that the angular momentum of the transferred mass evaluated by using the critical radius is added directly to the spin angular momentum of the accretor. Thus, the spin angular momentum transferred to the accretor is calculated as

$$\frac{dJ_{\text{sp},2}}{dt} = \dot{M}_2 \sqrt{GM_2 r_{\text{cri}}}. \quad (12)$$

Alternatively, if the transferred mass accretes through a disk, the spin angular momentum of the accretor increases assuming that the transferred mass falls onto the stellar surface of the accretor with the Keplerian velocity. Then the spin angular momentum transferred via the accretion disk is estimated as

$$\frac{dJ_{\text{sp},2}}{dt} = \dot{M}_2 \sqrt{GM_2 R_2}. \quad (13)$$

2.3 Common envelope

If the companion star plunges into the primary star which has a core and envelope structure due to an eccentric orbit, or mass transfer becomes dynamically unstable ($\zeta_L > \zeta_{\text{ad}}$), the binary becomes a common envelope phase. In this paper, we use the $\alpha\lambda$ formalism for calculating the common envelope phase evolution (Webbink 1984), and the orbital separation just after the common envelope phase a_f is calculated by the following energy budget if the accretor star is not a giant star,

$$\alpha \left(\frac{GM_{c,1}M_2}{2a_f} - \frac{GM_1M_2}{2a_i} \right) = \frac{GM_1M_{\text{env},1}}{\lambda R_1}. \quad (14)$$

Here, $M_{c,1}$ and $M_{\text{env},1}$ are the core and envelope mass of the donor star, M_2 is the mass of the accretor star and a_i is the separation just before the common envelope phase. The common envelope parameters are α and λ , where α is the parameter of the efficiency showing how much orbital energy is used to strip the stellar envelope, and λ is the parameter of the binding energy of the envelope.

When the accretor star is also a giant star, the orbital energy is used not only to strip the envelope of the donor star, but also to strip the envelope of the accretor star. In this case, the orbital separation just after the common envelope phase a_f is calculated as

$$\alpha \left(\frac{GM_{1c}M_{2c}}{2a_f} - \frac{GM_1M_2}{2a_i} \right) = \frac{GM_1M_{1\text{env}}}{\lambda R_1} + \frac{GM_2M_{2\text{env}}}{\lambda R_2}, \quad (15)$$

where M_{2c} , $M_{2\text{env}}$ and R_2 are the core and envelope mass and radius of accretor star.

2.4 Merged remnant and rotation effect

When the common envelope phase occurs, we estimate the separation just after the common envelope phase a_f , and check whether the binary has coalesced within the common envelope phase or not. When a_f is smaller than the sum of the remnant stellar radii, the binary has merged. Additionally, when the post-MS star does not reach the Hayashi track nor ignite helium burning, such a star, so-called a Hertzsprung gap star, might not have a clear core-envelope structure. In this case, we also assume the binary merges (Taam & Sandquist 2000; Belczynski et al. 2008). If a binary merges before

CCSNe, we treat the merged product as rapidly rotating with Kepler velocity.

Rapid rotation can enhance the material mixing inside the star. [Horiuchi et al. \(2021\)](#) showed the percentage increase of the carbon-oxygen (CO) core mass of pre-CCSN with respect to the non-rotating case, based on [Takahashi et al. \(2014\)](#); [Limongi \(2017\)](#). For massive stars with the zero-age main sequence mass $M_{\text{ZAMS}} > 13 M_{\odot}$, we consider the enhancing fraction of the CO core mass with respect to the non-rotating counterpart having the same total mass as

$$f_L = 53.4 M_{\text{ZAMS}}^{-3/2} + 0.847, \quad (16)$$

from Limongi's models ([Limongi 2017](#)). For $M_{\text{ZAMS}} < 13 M_{\odot}$,

$$f_T = 0.123 M_{\text{ZAMS}} + 0.392, \quad (17)$$

from Takahashi model ([Horiuchi et al. 2021](#)). Note that in all cases, if the CO core mass estimated by the above formulae exceeds the total stellar mass, we limit the CO core mass to the total stellar mass.

Just after the merger, the merged remnant has a high angular momentum, from the orbital angular momentum. We assume the angular momentum of merged remnant J_{merge} as the Kepler angular momentum. On the other hand, since the merged remnant loses angular momentum by the stellar wind mass loss, we consider the angular momentum mass loss described by

$$\Delta J = \frac{2}{3} \Delta M R^2 \Omega_{\text{spin}} = \frac{2}{3k} \frac{\Delta M}{M} J, \quad (18)$$

where ΔM is the stellar wind mass loss, M , R , Ω_{spin} , k , and J are the mass, radius, spin angular velocity, moment of inertia factor, and angular momentum of the merged remnant, respectively. We assume $k = 0.15$ which is the value of the red giant branch. The angular momentum of the merged remnant just before the SN is described as

$$J_{\text{preSN}} = J_{\text{merge}} \left(\frac{M_{\text{preSN}}}{M_{\text{merge}}} \right)^{\frac{2}{3k}}, \quad (19)$$

where M_{preSN} and M_{merge} are the total stellar mass of the merged remnant just before SN and the mass of the merged remnant just after the merger. We calculate the angular momentum of the CO core of the merged remnants just before SN as

$$J_{\text{CO}} = \frac{M_{\text{CO}} R_{\text{CO}}^2}{M_{\text{preSN}} R_{\text{preSN}}^2} J_{\text{preSN}}, \quad (20)$$

where M_{CO} and R_{CO} are the mass and the radius of the CO core, and R_{preSN} is the radius of the star just before SN. We estimate R_{CO} using the fitting formula,

$$R_{\text{CO}} = \frac{1.23 \times 10^{-3} + 8.06 \times 10^{-2} M_{\text{CO}} - 3.31 \times 10^{-3} M_{\text{CO}}^2}{1 + 0.467 M_{\text{CO}} - 3.03 \times 10^{-2} M_{\text{CO}}^2} R_{\odot}, \quad (21)$$

based on the mass-radius relation from [Giacobbo et al. \(2017\)](#).

2.5 Determination of SN Type

To study the SN explosions, we categorize the SN into six Types, based on the progenitor CO core mass (M_{CO}), angular momentum ($a_{\text{CO}}/M_{\text{CO}} = c J_{\text{CO}}/G M_{\text{CO}}^2$), and the presence of a Hydrogen envelope (see Table 1), extending the treatment in [Yoon et al. \(2006\)](#).

First, if the CO core mass is between $1.34 M_{\odot}$ and $5 M_{\odot}$, and the progenitor retains its hydrogen envelope, we classify them as Type

Table 1. SN types considered in this work.

SN type	CO core mass	a/M	Envelope type
AIC	$M_{\text{CO}} < 1.34 M_{\odot}$		WD
II	$1.34 M_{\odot} < M_{\text{CO}} < 5 M_{\odot}$		yes H
Ibc	$1.34 M_{\odot} < M_{\text{CO}} < 5 M_{\odot}$	< 1	no H
RSN	$1.34 M_{\odot} < M_{\text{CO}} < 5 M_{\odot}$	> 1	no H
BH	$5 M_{\odot} < M_{\text{CO}}$	< 1	either
GRB	$5 M_{\odot} < M_{\text{CO}}$	> 1	no H

II SNe, regardless of the angular momentum. Second and third involve the same CO core mass range but progenitors that have lost their hydrogen envelopes. If the angular momentum is less than 1 ($a_{\text{CO}}/M_{\text{CO}} < 1$) we classify them as Type Ibc SNs, while if the angular momentum is greater than 1 ($a_{\text{CO}}/M_{\text{CO}} > 1$) we classify them as Rapidly-rotating SNe (RSN). We expect the formation of rapidly rotating neutron stars, which may show different explosions from the normal SNe (MHD-driven explosion, see e.g., [Obergaullinger et al. 2014](#) or explosions driven by low- T/W instability, see e.g., [Takiwaki et al. 2021](#)). Fourth involves CO core masses less than 1.34 solar masses. If such progenitors undergo explosions due to accretion, they are designated as Accretion-Induced Collapse (AIC) SNe. Fifth and sixth concern progenitors with CO core masses greater than $5 M_{\odot}$. If $a_{\text{CO}}/M_{\text{CO}} < 1$, they are classified as Black Hole Formation events irrespective of the presence of a Hydrogen envelope or not. On the other hand, if $a_{\text{CO}}/M_{\text{CO}} > 1$ and there are no Hydrogen envelope, they are identified as GRBs. We assume that if the star with high angular momentum has a Hydrogen envelope, it loses the angular momentum due to efficient mass loss, and it cannot explode as GRB or RSN.

We should keep in mind the limitation of such a simple classification. [Patton et al. \(2022\)](#) employ more complex criteria ([Fryer et al. 2012](#); [Ertl et al. 2016](#)) and the results are shown in their Fig. 4. Though the bifurcation of NS and BH is not the sole function of M_{CO} , we still see some general trend that BH appears where $M_{\text{CO}} > 5 M_{\odot}$. [Schneider et al. \(2021\)](#) employ the criteria of [Müller et al. \(2016a\)](#). In their Fig. 7, BH appears in $7 M_{\odot} < M_{\text{CO}} < 8 M_{\odot}$ and $14 M_{\odot} < M_{\text{CO}}$. [Burrows et al. \(2020\)](#) and other studies claim that black holes tend to appear in a mass range of $13 M_{\odot} < M_{\text{ZAMS}} < 15 M_{\odot}$, which correspond to $2 M_{\odot} < M_{\text{CO}} < 3 M_{\odot}$. Such new scenarios should be tested in the future.

It is hard to estimate the angular momentum of the final compact object, WD, NS, or BH from the angular momentum of the CO core. This study treats the angular momentum in a qualitative way. Here, we introduce a simple treatment in the previous studies for further improvement. The angular momentum of CO core can be distributed to the central objects and accretion disks. See Section 8.3.4 in [Fragos et al. \(2023\)](#) for this issue. Numerical simulations would be also useful to map the angular momentum from the core to the compact object ([Sekiguchi & Shibata 2011](#); [Fujibayashi et al. 2023](#)).

3 MODELS & CALCULATION RESULTS

3.1 Parameter survey

We first conduct a parameter survey of solar metal binary evolution, by performing binary evolution calculations with fixed mass ratios, $q = M_2/M_1$, and binary parameters in circular orbits. We explore the impacts of initial mass and initial separation on binary evolution and how it influences SN outcomes. We calculate three fixed mass

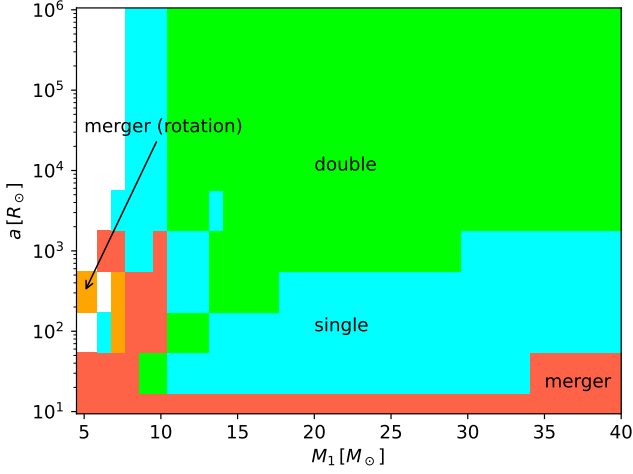


Figure 1. The binary progenitors of SNe in the mass ratio $q = 0.7$ case. Here, “double” and “single” refer to binary systems where both stars are core-collapse progenitors and where only one of the stars are core-collapse progenitors, respectively. Binary systems where the stars merge before core collapse are labeled “merger”. Systems that merge and create a light mass star that only core collapse after considering rotation effects are labeled “merger (rotation)”. See text for details.

ratio models, $q = 0.5, 0.7,$ and 0.9 . In each model, we calculate the initial mass from $3 M_{\odot}$ to $100 M_{\odot}$ and the initial separation a_{ini} from $10 R_{\odot}$ to $10^6 R_{\odot}$. The initial eccentricity is set to zero. We assume $\beta = 1, \alpha\lambda = 1,$ and no pulsar kick.

In this section, we focus on the $q = 0.7$ model, and describe the $q = 0.5$ and $q = 0.9$ models in Appendix B. Figure 1 shows the progenitor of the SN. If SN progenitors do not merge before the core collapse, we split these into binary systems where both stars are core-collapse progenitors (double) and binary systems where only one of the stars are core-collapse progenitors (single). If the binary stars merge before core collapse, we split these into binary systems where the progenitors become core-collapse progenitors as a result of rotational effects (merger rotation), and binary systems where the progenitor become core-collapse progenitors independently of rotational effects (merger) (see Horiuchi et al. 2021, for similar classification).

Binary calculations with $a = 10^6 R_{\odot}$ are effectively single stellar evolutions. However, when the initial separation is less than $\sim 10^4 R_{\odot}$, the SN progenitors can interact with the companion star and qualitatively change the SN progenitors. Figure 1 shows that the influence of binary interactions depends strongly on the evolution separation. In the range $a \simeq 10^{1.5} R_{\odot}$ to $a \simeq 10^3 R_{\odot}$, a massive binary where both stars are originally expected to undergo SNe becomes a single core-collapse system due to binary interactions. After the primary star become a SN or a core collapse, the secondary star reaches the Hertzsprung gap and makes a common envelope with the primary compact object. At that time, the secondary star disappears due to merging with the primary compact object during the common envelope phase. In the range $a \lesssim 10^{1.5} R_{\odot}$, a massive binary will merge due to binary interactions before a SN. In particular, even if the primary star starts with a mass lower than the criterion for SN explosion, the binary interaction can enable it to become a SN. We see this new channel appear for close binaries $a \lesssim 10^3 R_{\odot}$. The effect of rotation amplifies this effect by increasing the core mass by mixing (Horiuchi et al. 2021).

In Figs. 2 and 3, we show the fates of the primary star and the sec-

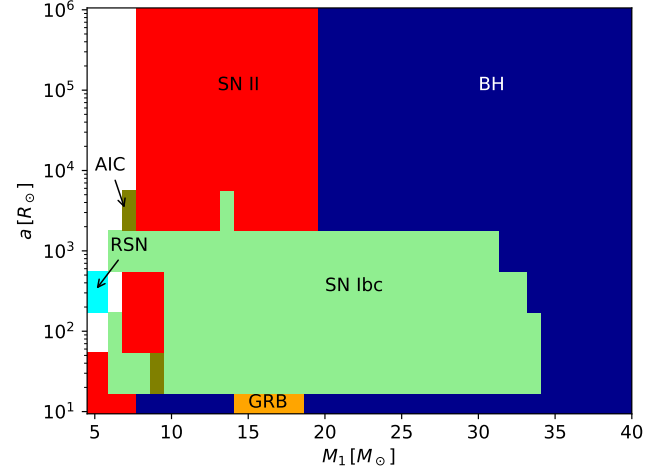


Figure 2. SN type of primary star in the $q = 0.7$ case. See Table 1 for SN type classifications.

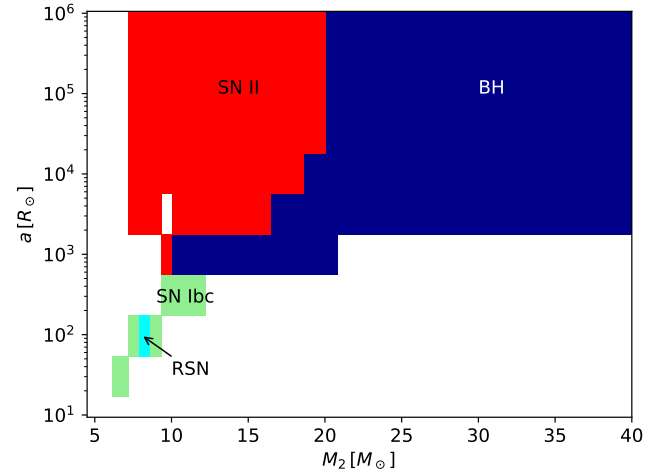


Figure 3. SN type of secondary star in the $q = 0.7$ case. Note that the results of merged stars are omitted here and shown instead in Fig. 2. The parameter region shown is thus limited to the double system labeled in Fig. 1.

ondary star, respectively, as functions of the ZAMS mass and binary separation. For the secondary, white regions with close separation represent cases where mass is lost in the common envelope phase and the secondary star does not experience core collapse. If the SN progenitor is effectively a single star ($a_{\text{ini}} \gtrsim 10^4 R_{\odot}$), they evolve only to Type II SN or BH, depending on the CO core mass. Figures 4 and 5 show the CO core mass as functions of the ZAMS mass and binary separation, illustrating this dependence. In the high separation regime, the CO core mass is determined solely by the initial mass, with a larger initial mass leading to a larger CO core mass. When M_1 or M_2 becomes larger than $\sim 20 M_{\odot}$, M_{CO} becomes $\geq 5 M_{\odot}$ and BH is formed in our classification. The angular momentum of the CO core is negligible in the case of effectively single stellar evolution, because the majority of the angular momentum is held by the hydrogen envelope, and there is angular momentum loss due to stellar wind mass loss. We can confirm this in Figs. 6 and 7, where we show the angular momentum as functions of the ZAMS mass and binary separation.

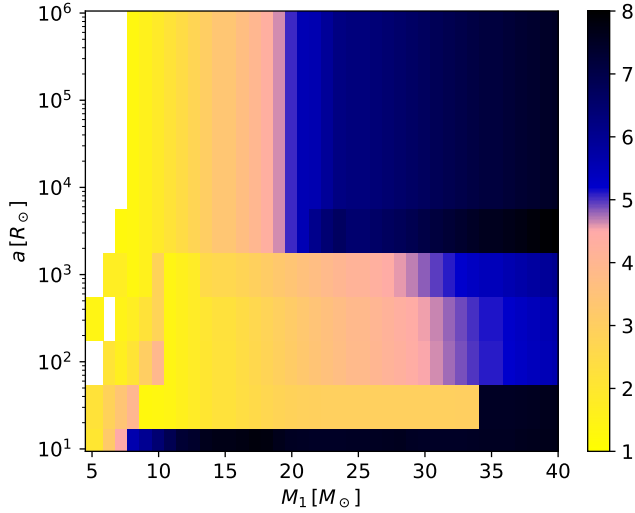


Figure 4. CO core mass of primary star in the $q = 0.7$ case.

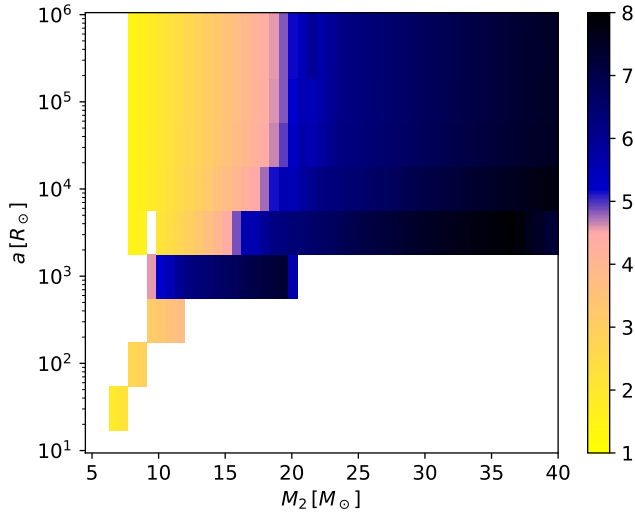


Figure 5. CO core mass of secondary star in the $q = 0.7$ case.

Fragos et al. (2023) shows similar results. In their Fig. 4, M_{CO} is shown as a function of M_{ZAMS} . In the range of $M_{\text{ZAMS}} < 40 M_{\odot}$, M_{CO} almost linearly increases and is consistent with our results. In their Fig. 30, BH appear $20 M_{\odot} < M_1$, which is consistent with our results. They use slightly different classifications of the fate of massive stars. In their Fig. 29, they also classify electron capture SN with the criterion of $1.37 M_{\odot} < M_{\text{CO}} < 1.43 M_{\odot}$. In this paper, we do not focus on these kinds of SNe (see Fig. 2). They also consider pair-instability SN and pulsational pair-instability SN with certain criteria. Those SNe should appear in more massive stars, $M_{\text{ZAMS}} > 50 M_{\odot}$, and does not affect our results. Note that in a higher mass range, $M_{\text{ZAMS}} > 30 M_{\odot}$, the value of M_{CO} significantly depends on the mass loss prescription of Wolf-Rayet stars (see also Fig. 1 of Patton et al. 2022).

If a binary is close enough so that the binary interaction is effective, more complex behavior is exhibited. In the parameter region of $10^{1.5} R_{\odot} < a < 10^{3.5} R_{\odot}$, a SN progenitor becomes a Type Ibc SN due to mass loss by binary interactions. One typical evolution-

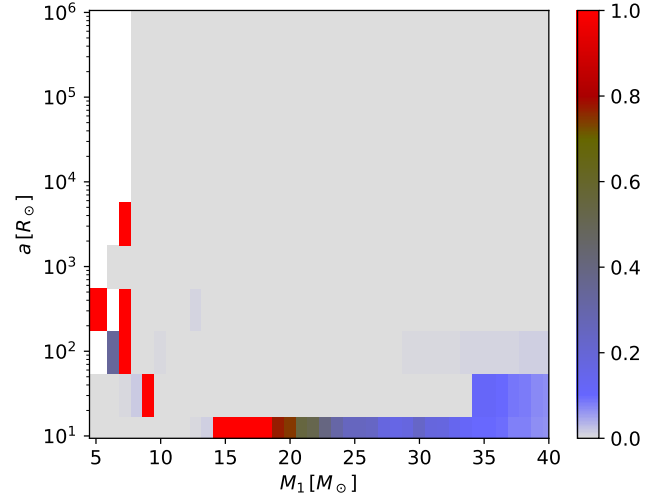


Figure 6. Angular momentum of primary star in the $q = 0.7$ case.

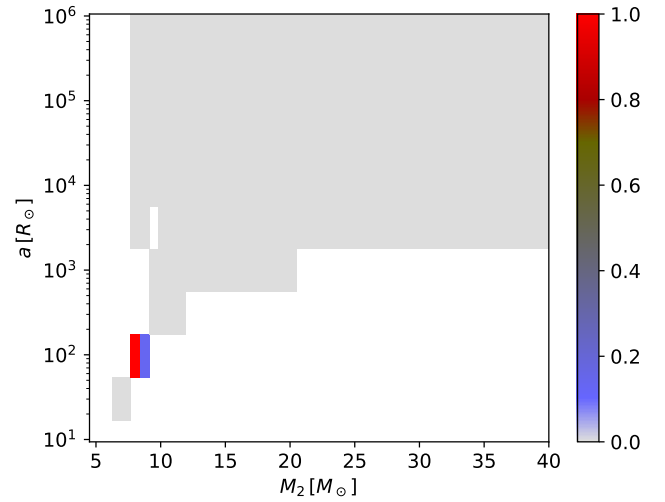


Figure 7. Angular momentum of secondary star in the $q = 0.7$ case.

ary path of Type Ibc SN progenitors is shown in Fig. 8. Since the primary star and the secondary star lose their envelopes via mass transfer and common envelope phase, respectively, they can become type Ibc SN due to mass loss. Another consequence is that binary effects reduce the M_{CO} of the primary; see Fig. 4 and compare M_{CO} in $10^{1.5} R_{\odot} < a < 10^{3.5} R_{\odot}$ to that in $10^{3.5} R_{\odot} < a$. At $M_1 \sim 20 M_{\odot}$, $M_{\text{CO}} \sim 2\text{--}3 M_{\odot}$ for $10^{1.5} R_{\odot} < a < 10^{3.5} R_{\odot}$ but $M_{\text{CO}} \sim 5 M_{\odot}$ in $10^{3.5} < a$.

These results are consistent with Schneider et al. (2021). In their Fig. 3, Case A and Case B mass transfer makes the core mass lighter. The effect of mass transfer on the secondary star is complicated. See Fig. 5, at $a \sim 10^3 R_{\odot}$ and $10 M_{\odot} < M_2 < 20 M_{\odot}$, the core mass is increased by the mass transfer from the primary star. In the region with smaller a and M_2 , core mass is also increased due to the same reason. Note that the parameter regions of the figure are limited and correspond to the double in Fig. 1.

If a binary is close enough to merge, there are generally two main scenarios, depending on the evolutionary stage of the primary star. If the primary star has already become a compact object, the

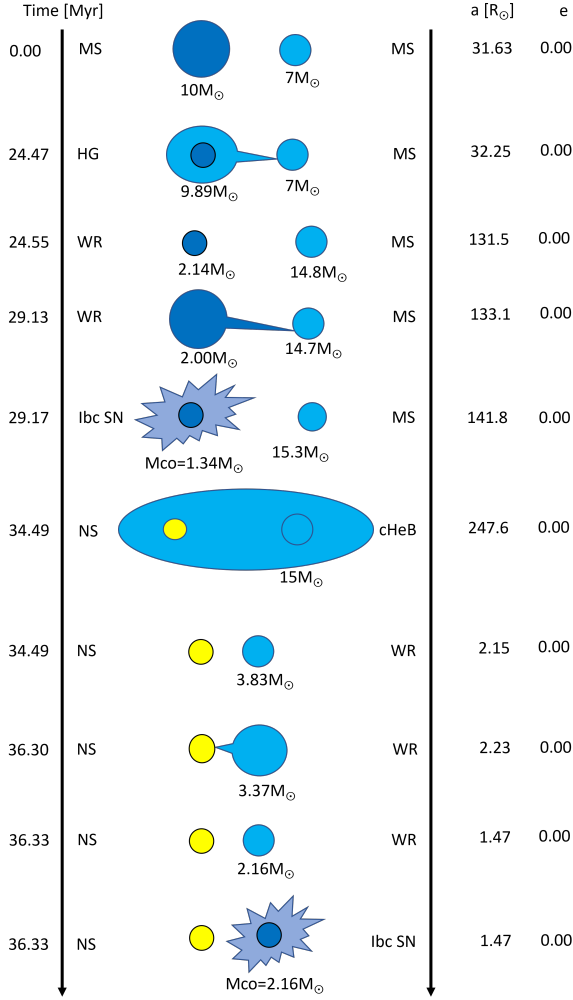


Figure 8. Example of the Type Ibc SN progenitor evolutionary path. MS, HG, WR, and cHeB are main sequence, Hertzsprung gap, Wolf-Rayet star, and helium core burning phase, respectively.

secondary star disappears through merging with the primary compact object. In the range $a \simeq 10^2 R_\odot$ to $a \simeq 10^3 R_\odot$, a massive binary where both stars were originally expected to undergo SNe therefore only experience one SN due to the merger. On the other hand, if the primary star is not a compact object, the merger creates a rapidly rotating star. The CO core of the merged remnant tend to be increased by the rotation effect. Subsequently, part or most of the angular momentum of the merged remnant can be lost by stellar wind mass loss.

Merged remnants that lose their hydrogen envelope due to stellar winds while retaining sufficient angular momentum until the time of their explosion can lead to GRBs. Note that [Fragos et al. \(2023\)](#) stop their simulation after the merger, and we cannot compare results. GRBs appear in a limited parameter range, $a = 10 R_\odot$ and $M_1 \sim 15 M_\odot$, as see in Fig. 2. We show the main channel for the birth of GRB progenitors in Fig. 9. Typically, GRB progenitors gain huge angular momenta from a binary merger. If the mass of the merged progenitors is relatively massive, angular momentum loss due to strong stellar wind mass prevents the occurrence of a GRB. On the other hand, if the mass of merged progenitors is relatively low mass, they can evolve while retaining angular momentum until just before

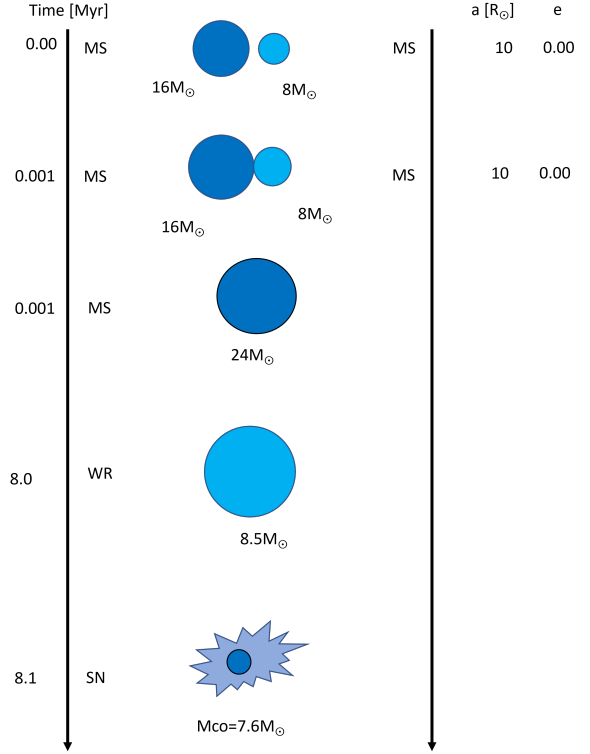


Figure 9. Example of the GRB progenitor evolutionary path.

the gravitational collapse. Thus, systems whose mass $M_1 \sim 15 M_\odot$ can undergo gravitational collapse while retaining sufficient angular momentum of the CO core. If the merged progenitor mass is too low ($M_1 \leq 14 M_\odot$), they can collapse with a hydrogen envelope. In this case, the star is a giant with a large radius, causing the majority of the angular momentum to be held by the envelope rather than the CO core. Hence, not only is it unable to produce a GRB, the angular momentum of the core also becomes significantly reduced (See Fig. 6).

We found two parameter regions for a Rapidly-rotating SN (RSN), i.e., $(M_1, a) = (5 M_\odot, 10^{3.5} R_\odot)$ in Fig. 2 and $(M_2, a) = (7 M_\odot, 10^2 R_\odot)$ in Fig. 3. We show the two pathways in Fig. 10. One of them is through a merger. For instance, in the left-hand side of Fig. 10, a binary system with an initial mass of 5 solar masses and an initial orbital semi-major axis of $a = 10^{2.5} R_\odot$ evolves into a binary system composed of a White Dwarf (WD) and a Red Giant (RG). After the binary merger, the remaining Wolf-Rayet (WR) star undergoes a SN explosion. Because the binary merger allows for the retention of a significant amount of angular momentum, it can lead to a RSN. In the right-hand side of Fig. 10, the second pathway involves the binary evolution leading to a very close binary system (a of a few R_\odot), such as a NS-WR binary, in the late stages. In this scenario, the secondary star undergoes rapid rotation due to tidal effects, and it eventually explodes as a RSN. In both cases, the core mass is not so large, i.e., $M_{\text{CO}} = 1.44 M_\odot$ or $2.65 M_\odot$. It is interesting to note that heavier stars are often employed in simulations, e.g., $(M_{\text{ZAMS}}, M_{\text{CO}}) = (27 M_\odot, \sim 7 M_\odot)$ in [Takiwaki et al. \(2021\)](#); $(M_{\text{ZAMS}}, M_{\text{CO}}) = (35 M_\odot, 20\text{--}30 M_\odot)$ in [Obergaullinger & Aloy \(2020\)](#). Although lighter stars are also considered

$(M_{\text{ZAMS}}, M_{\text{CO}}) = (5 M_{\odot}, 4 M_{\odot})$ in [Obergaullinger & Aloy \(2022\)](#), it is still heavier than what we observe due to binary effects.

There are two parameter regions corresponding to an accretion-induced collapse (AIC), see $(M_1, a) \sim (7 M_{\odot}, 3000 R_{\odot})$ and $(9 M_{\odot}, 30 R_{\odot})$ in Fig. 2. The two pathways are shown in Fig. 11. One of them is that the primary star, whose initial mass is lower than the SN criterion (in single stellar evolution case), becomes an AIC due to mass accretion from the secondary star. The other is the case where the primary star's initial mass is more massive than the SN criterion mass (in single stellar evolution case), but it loses a lot of mass via mass transfers and it cannot become a SN. However, it can become an AIC due to mass accretion from the secondary star. Interestingly, the angular momentum of the core is high in both case, see Fig. 6 and the points $(M_1, a) \sim (7 M_{\odot}, 3000 R_{\odot}), (9 M_{\odot}, 31.30 R_{\odot})$. Recently, simulations of AIC were performed (e.g., [Mori et al. 2023](#)) and the effect of rotation is considered ([Abdikamalov et al. 2010](#); [Longo Micchi et al. 2023](#)).

3.2 Population synthesis calculation

3.2.1 Initial parameter distribution and binary parameters

We conduct Binary Population Synthesis calculations for 12 models by varying the initial parameter distributions and binary evolution parameters with solar metallicity. The differences between the 12 models are combinations of variations in the initial condition distribution of binary systems, mass transfer parameter β , and common envelope parameters $\alpha\lambda$. Table 2 shows the parameters for our 12 models. For each model, we performed calculations for 10^5 binary systems.

Each initial condition model uses the same initial mass function (IMF) and the same initial mass ratio function (IMRF). We adopt the Salpeter IMF,

$$f(M) = M^{-2.35}, \quad (22)$$

from $3 M_{\odot}$ to $100 M_{\odot}$ [Salpeter \(1955\)](#), and the flat IMRF from [Kobulnicky & Fryer \(2007\)](#),

$$f(q) = \text{const}, \quad (23)$$

from 0 to 1, where $q = M_2/M_1$. In the case of the initial orbit parameter distributions such as separation (period) and eccentricity, we use two initial conditions. One is the initial orbit condition distributions from [Sana et al. \(2012\)](#). In order to calculate the separation in this model, we use the initial period P function,

$$f(\log P) = \left(\log \left[\frac{P}{\text{day}} \right] \right)^{-0.55}, \quad (24)$$

from $\min[10^{0.15} \text{day}, P_{\min}]$ to $(P/\text{day}) = 10^{3.5}$, where P_{\min} is the minimum period where the binary does not interact, and use the initial eccentricity function,

$$f(e) = e^{-0.5}, \quad (25)$$

from 0 to 1. The other model adopts the orbital initial conditions by [Abt \(1983\)](#); [Heggie \(1975\)](#). In this model, we use the log flat separation distribution,

$$f(a) = \frac{1}{a}, \quad (26)$$

from a_{\min} to $10^6 R_{\odot}$, where a_{\min} is the minimum separation where the binary does not interact, and use the initial eccentricity function

$$f(e) = e, \quad (27)$$

Table 2. Parameters for our 12 binary synthesis models.

model	Initial orbit population	β	$\alpha\lambda$
Sana_MT1_CE01	Sana et al. (2012)	1	0.1
Sana_MT1_CE1	Sana et al. (2012)	1	1
Sana_MT1_CE10	Sana et al. (2012)	1	10
Sana_MT05_CE01	Sana et al. (2012)	0.5	0.1
Sana_MT05_CE1	Sana et al. (2012)	0.5	1
Sana_MT05_CE10	Sana et al. (2012)	0.5	10
Abt_MT1_CE01	Abt (1983) ; Heggie (1975)	1	0.1
Abt_MT1_CE1	Abt (1983) ; Heggie (1975)	1	1
Abt_MT1_CE10	Abt (1983) ; Heggie (1975)	1	10
Abt_MT05_CE01	Abt (1983) ; Heggie (1975)	0.5	0.1
Abt_MT05_CE1	Abt (1983) ; Heggie (1975)	0.5	1
Abt_MT05_CE10	Abt (1983) ; Heggie (1975)	0.5	10

from 0 to 1.

For the mass transfer parameter β , we use 0.5 and 1. Here, $\beta = 1$ is a conservative mass transfer. On the other hand, $\beta = 0.5$ means that half of the transferred matter can be accreted to the companion star, and the rest is released out of the binary system.

We use 0.1, 1, and 10 as the combination of the common envelope parameters $\alpha\lambda$. When the common envelope parameter values are small, it means that there is less energy available to expel the envelope efficiently during the common envelope phase. As a result, the separation between the two stars tends to decrease because they remain closer together within the common envelope phase. Conversely, when the common envelope parameter values are large, it indicates that more energy is available to expel the envelope. This can lead to a more effective expulsion of the envelope, allowing the two stars to separate further from each other after the common envelope phase.

3.2.2 Results of population synthesis calculation

Table 3 shows the results of our 12 binary synthesis models, listing the numbers of each SN Type in 10^5 binaries. The main difference between the Sana initial orbit models and the Abt initial orbit models is the numbers of Type II and Type Ibc SNe. The fraction of close binaries is much higher in the Sana initial orbit models. Close binaries are more likely to become Type Ibc SNe and less likely to become Type II SNe (See Fig. 2). Thus, the number of Type Ibc SN is much higher in the Sana initial orbit models.

The mass transfer parameter β impacts strongly the number of AIC. Since AIC is caused by accretion, the small β which reduces the mass transfer generally makes binaries harder to become AIC.

The common envelope parameter $\alpha\lambda$ influences the number of mergers, with smaller $\alpha\lambda$ increasing binary mergers. Thus, there is a monotonic increase in the number of GRB with small $\alpha\lambda$. However, for AIC and RSN cases, the number of events peaks at $\alpha\lambda = 1$, and decrease both as $\alpha\lambda$ is decreased or increased. Particularly, at $\alpha\lambda = 0.1$, the number of events decreases significantly. This is because both AIC and RSN scenarios require the binary separation to be reduced through a common envelope phase. When the primary star initiates the common envelope phase, and if $\alpha\lambda$ is too small, more binaries tend to merge at that stage. On the other hand, if $\alpha\lambda$ is too large, it does not shrink the orbit much, leading to a slight decrease in the likelihood of forming close binary systems later on. The sharp increase in the number of Type II SNe and the sharp decrease in the number of Type Ibc SNe when $\alpha\lambda = 0.1$ are attributed to an increase in binaries that fail to effectively shed the envelope during the common envelope phase and consequently merge. After

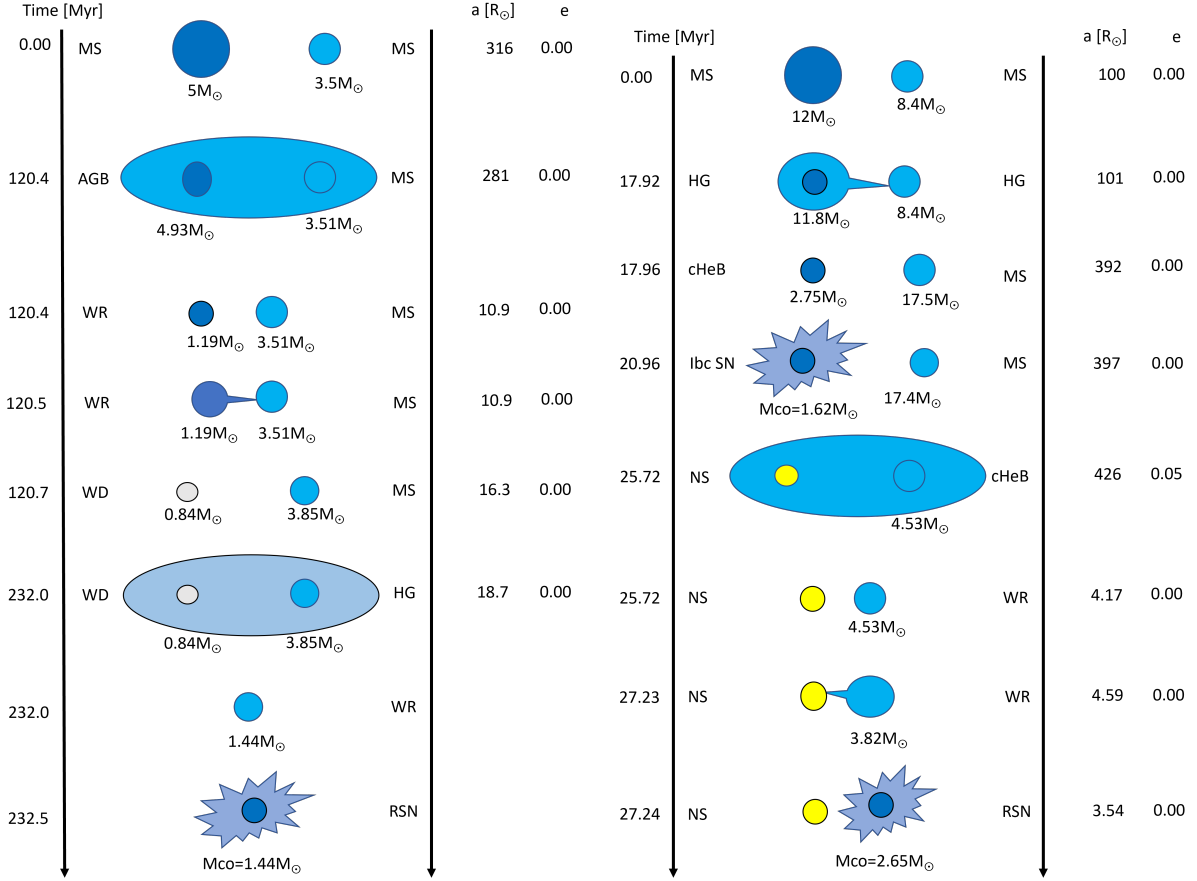


Figure 10. Examples of RSN progenitor evolutionary paths. The case for $q = 0.7$ is shown. We have found another example as in Fig. B12 for $q = 0.9$.

Table 3. The numbers of each SN type for our 12 models. The number of binaries per model is 10^5 .

model	AIC	Ibc	II	RSN	BH	GRB
Sana_MT1_CE01	31	6780	32646	75	14726	912
Sana_MT1_CE1	794	26456	16460	1298	11412	729
Sana_MT1_CE10	438	26322	12015	1261	10551	678
Sana_MT05_CE01	57	6769	30314	60	11719	897
Sana_MT05_CE1	189	20189	17619	1515	9677	701
Sana_MT05_CE10	138	24598	11432	1949	8740	663
Abt_MT1_CE01	210	2564	30560	71	12638	638
Abt_MT1_CE1	451	11222	24659	546	10565	427
Abt_MT1_CE10	517	10515	22003	504	9976	390
Abt_MT05_CE01	265	2678	30258	62	11950	629
Abt_MT05_CE1	276	9453	24776	608	10107	416
Abt_MT05_CE10	356	9933	21831	644	9549	389

the merger, the presence of the remaining envelope makes it more likely for the star to become a Type II SN.

In order to calculate the fractions of each SN type for our 12 models, we assume a binary fraction f_b of 70% (e.g., Sana et al. 2012) and $f_b=50\%$ (e.g., Tian et al. 2018). According to Fig. 2, for effectively single stars, relatively light stars ($8M_\odot < M < 20M_\odot$) tend to become Type II SN, while more massive stars ($> 20M_\odot$)

tend to become BH. If $f_b=70\%$ (50%), the number of Type II SN and the number of BH increase to 8163 (19049) and 2959 (6903), respectively. Figures 12 and 13 show the fractions of each SN type for our 12 models with $f_b = 70\%$ and $f_b = 50\%$, respectively. The numerical data are provided in Appendix C.

Observations of SN at low redshifts reveal that the fraction of SN types is approximately II:Ibc = 75:25 (Li et al. 2011). We show in Figures 14 and 15 the II:Ibc ratio for each of our 12 model with $f_b = 70\%$ and $f_b = 50\%$, respectively. Among the models we calculated, the Abt_MT05_CE10 model with $f_b = 70\%$ best matches observations. The next best-fitting model is the Abt_MT1_CE1 model with $f_b = 70\%$. In the models using Sana et al. (2012) initial parameters, we find that due to a higher number of close binary systems, there is a tendency for more Type Ibc SNe compared to Type II SNe, in comparison to the models using Abt (1983); Heggie (1975) initial parameters.

The local SN rate in our galaxy R_{SN} can be calculated as,

$$R_{\text{SN}} = \frac{\int_3^{100} M^{-2.35} dM N_{\text{Ibc}} + N_{\text{II}} + N_{\text{RSN}} \text{SFR}_{\text{gal}}}{\int_0.1^{100} M^{-2.35} dM (2N_{\text{binary}} + N_{\text{single}}) \langle M \rangle}, \quad (28)$$

where N_{Ibc} , N_{II} , and N_{RSN} are the numbers of Type Ibc SN, Type II SN, and RSN, respectively. N_{binary} and N_{single} are the numbers of total binary systems and single star systems, respectively. SFR_{gal} and $\langle M \rangle$ are the star formation rate of our galaxy (assumed $2M_\odot \text{ yr}^{-1}$), and the average mass of stars, respectively. In our simulation, we find R_{SN} falls from $1.14 \times 10^{-2} \text{ yr}^{-1}$ to $1.57 \times 10^{-2} \text{ yr}^{-1}$. These values

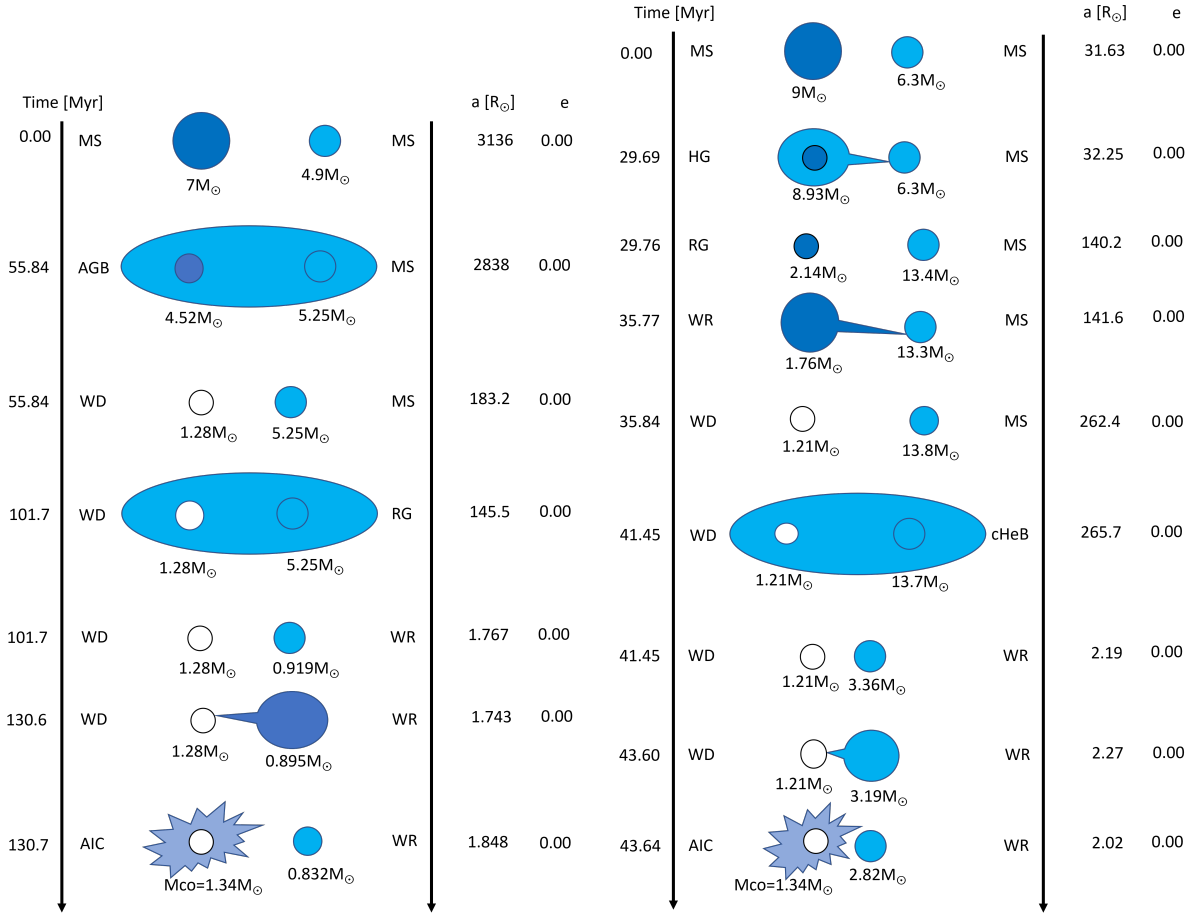


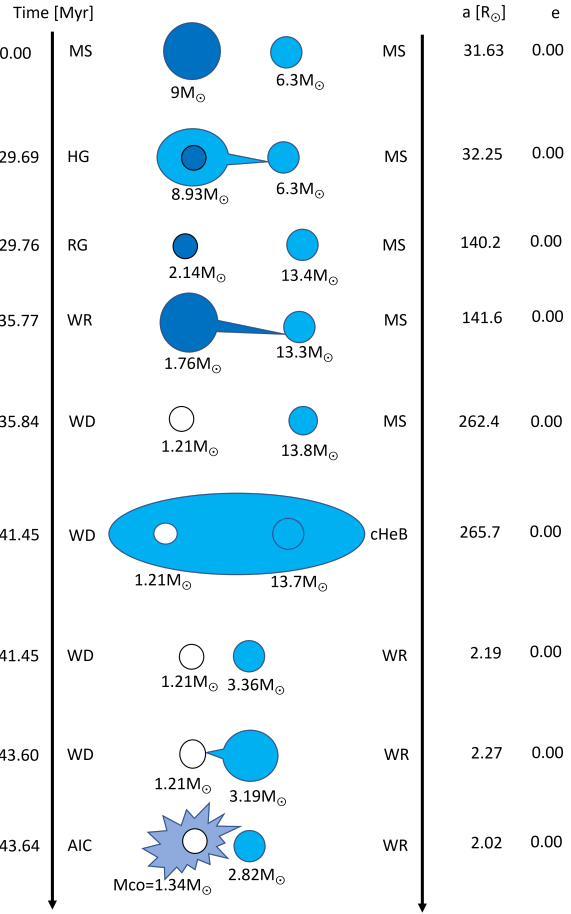
Figure 11. Examples of AIC progenitor evolutionary paths.

are consistent with the core collapse SN rate in our galaxy from observation, $R_{\text{SN,obs}} = 3.2^{+7.3}_{-2.6} \times 10^{-2} \text{ yr}^{-1}$ (Adams et al. 2013).

The local GRB rate at $z \sim 0$ can be calculated as,

$$R_{\text{GRB}} = f_B \frac{\int_3^{100} M^{-2.35} dM}{\int_{0.1}^{100} M^{-2.35} dM} \frac{N_{\text{GRB}}}{2N_{\text{binary}} + N_{\text{single}}} \frac{\text{SFR}}{\langle M \rangle}, \quad (29)$$

where f_B , N_{GRB} , and SFR are the beaming factor of long GRB ($f_B = 0.01$ estimated in Liang et al. 2008; Kinugawa & Asano 2017; Kinugawa et al. 2019), the number of GRB, and the star formation rate at $z \sim 0$ (SFR = $10^{-1.82}$ estimated in Wyder et al. 2005; Madau & Dickinson 2014), respectively. We find that the long GRB rate of our models is from $5.61 \text{ yr}^{-1} \text{ Gpc}^{-3}$ to $16.3 \text{ yr}^{-1} \text{ Gpc}^{-3}$. On the one hand, the local long GRB rate from the GRB observation is $1.3^{+0.6}_{-0.7} \text{ yr}^{-1} \text{ Gpc}^{-3}$ (Wanderman & Piran 2010), much lower than our estimates. On the other hand, observations suggest that there are many long GRBs with lower luminosities that are harder to detect (Pian et al. 2006), and the long GRB rate $1.3^{+0.6}_{-0.7} \text{ yr}^{-1} \text{ Gpc}^{-1}$ (Wanderman & Piran 2010) only includes the “normal” long GRBs with high luminosity $L > 10^{49} \text{ ergs s}^{-1}$. The low luminosity long GRB rate is estimated $R_{\text{LLGRB}} \sim 100\text{--}600 \text{ yr}^{-1} \text{ Gpc}^{-1}$ (Pian et al. 2006; Liang et al. 2007). If we assume that all GRB progenitors of our models become a low luminosity long GRB, then we estimated the low luminosity long GRB rate from $40.1 \text{ yr}^{-1} \text{ Gpc}^{-1}$ to $116 \text{ yr}^{-1} \text{ Gpc}^{-1}$ using a beaming factor for low luminosity long GRB $f_B = 1/14$ (Liang et al. 2007). According to Liang et al. (2007), it is possible



that f_B of a low luminosity long GRB is greater than $1/14$. In this case, this rate could become even larger. Thus, the low luminosity long GRB rates of our models are roughly consistent with the low luminosity GRB rate from observations.

Based on our population synthesis models, we are able to estimate the rates of RSN and AIC. To the best of our knowledge, this is the first time for the RSN rate to be estimated. Shibagaki et al. (2020) assume GRB rates as a proxy for the rate and we confirm that assumption is not wrong. In the best-fit models (Abt_MT05_CE10 model or Abt_MT1_CE1 model), the rate is close to the GRB rate. Though it is a rare opportunity, we can expect neutrino and gravitational waves from nearby RSN, which would have time-variability of the frequency of proto-neutron star (e.g., Takiwaki et al. 2021). Note that the rate strongly depends on the common envelope parameter. As discussed above, in the models with $\alpha\lambda = 0.1$, the rate significantly drops. The rate of AIC is similar to RSN.

We can also obtain the NS:BH ratios from our calculations. In all models, the NS:BH fraction remains relatively constant, ranging from 79:21 to 72:28. These values are approximately the same as a single star case (NS:BH=73:27) if we assume that progenitors with $8 M_{\odot} \leq M \leq 20 M_{\odot}$ become type II SNe (NSs) and progenitors with $20 M_{\odot} < M$ become BHs. These are broadly consistent with observations. In particular, there are a few candidate massive stars that have disappeared without obvious luminous SNe (Gerke et al. 2015; Adams et al. 2017a,b; Basinger et al. 2021; Neustadt et al.

2021). If these are collapses to black holes, they can be combined with the number of disappearances coincident with SNe to yield the fraction of core collapses that fail to produce SNe (Kochanek et al. 2008). Current estimates of such a black hole channel is $23.6^{+23.3}_{-15.7}\%$ of massive stars undergoing collapse. Other indirect probes also indicate similar fractions (e.g., Horiuchi et al. 2014).

4 SUMMARY AND DISCUSSION

In this paper we aim to systematically investigate how binary interactions affect the progenitors of SNe. To this end, we first conducted binary evolution calculations with fixed mass ratios. With this setup, we explored the orbital separations and primary star masses where various types of SNe can be produced, and delineated the evolutionary pathways through which each SN explosion could occur. We found that binaries with orbital separation greater than the red giant radius evolve similarly to single stars. Relatively lighter stars in such binaries become Type II SNe, while heavier stars become BHs. On the other hand, we found that binaries with orbital separations roughly equal to or less than the red giant’s radius develop into diverse types of SNe due to binary interactions, such as a common envelope phase and/or stable mass transfer. Rare explosion phenomenon such as rapidly rotating SNe and accretion induced collapse (AIC) are also observed in this separation range, $10^{1.5} R_{\odot} < a < 10^{3.5} R_{\odot}$ with lighter mass progenitor $M_{ZAMS} < 9 M_{\odot}$. Furthermore, we found that binaries with orbital separation $\lesssim 10 R_{\odot}$ undergo stellar mergers before core collapse. This implies that such progenitor stars have relatively large angular momentum at core collapse, making them conducive as long GRB progenitors.

In a previous study, Kinugawa & Asano (2017) calculated the long GRB rate of binary merger progenitor models (Fryer & Heger 2005). In their binary merger progenitor model, the stellar merger of naked He stars or the stellar mergers of naked He star and red giant as the long GRB progenitor were considered. Kinugawa & Asano (2017) showed that the long GRB rate by the binary merger progenitor model is consistent with the long GRB rate from observation (Wanderman & Piran 2010), and the metallicity evolution effect to the binary merger progenitor model can explain the evolution of the redshift of the long GRB rate. In our study, however, there is no long GRB progenitor of the binary merger progenitor model. The reason for this difference lies in the different treatments of the envelopes of the remnants that merged during the common envelope phase. In Kinugawa & Asano (2017), it was assumed that all the envelope will evaporate after the common envelope phase due to the huge angular momentum by the merger. On the other hand, we assumed that the envelope is not completely blown away during the common envelope phase, and partially remains. The binary merger progenitor model considers the merging of He stars in the late stages of evolution, which implies that they might have more angular momentum compared to our model, where stars merge early in the main sequence and lose angular momentum due to stellar winds. Furthermore, the binary merger progenitor model calculation (Kinugawa & Asano 2017) is consistent with the normal long GRB rate, whereas our calculation models appear to be consistent with low luminosity long GRBs rather than normal long GRBs. Therefore, it is plausible that the formation processes of normal long GRBs and low luminosity long GRBs are different.

In our calculations, close binaries tend to lead to Type Ibc SNe. Therefore, the models with Sana et al. (2012) initial parameters typically showed larger discrepancies in the ratio between Type Ibc and Type II SNe compared to observations, with an overabundance

of Type Ibc SNe. While this can be offset with a lower common envelope parameter, which results in increased number of remnants merging within the common envelope and a significant increase in the number of Type II SNe, this outcome is highly dependent on the handling of the envelopes of the merging remnants in the process. If we assume the same hypothesis of Kinugawa & Asano (2017), the number of Type II SNe could decrease in this case. To increase the number of Type II SNe in the Sana et al. (2012) initial parameter models, several factors might be needed, e.g., an increase in the number of single stars, an increase in binaries with significantly wider separations where interactions don’t play a significant role, or making the stripping of the hydrogen envelope by common envelope interactions less effective than it is now.

Binary population models like ours holds various possible applications. For example, there are growing numbers of observations of neutron stars (see Enoto et al. 2019, and references therein). Previous studies have revealed valuable insights into the distributions of mass, rotation, magnetic fields, and kicks (e.g., Noutsos et al. 2013; Igoshev et al. 2022). Though this paper does not discuss neutron star properties, it is important to compare our theoretical models with observations. Recently, the correlation of neutron star spins and spin-kick alignment is discussed in Janka et al. (2022).

Also, since we calculate the number of explosive phenomena and CO core mass of the progenitor, our models allow for an updated prediction of DSNB flux such as previously demonstrated in Horiuchi et al. (2021). The DSNB is a promising method to investigate the properties of extragalactic core collapses (Beacom 2010; Lunardini 2016; Ando et al. 2023). The SuperKamiokande (SK) water Cherenkov detector has already excluded some theoretical models and placed upper bounds on the DSNB flux (Abe et al. 2021). Recently, SK was upgraded with a gadolinium salt (SK-Gd), and expected to perform significantly more sensitive searches for the DSNB (Harada et al. 2023). On the theoretical side, more realistic predictions of DSNB is ongoing. For example, Horiuchi et al. (2021) and Kresse et al. (2021) consider the binary effect. Ashida et al. (2023) uses a new modeling of galactic chemical evolution, where a variable stellar initial mass function depending on the galaxy type. Ekanger et al. (2022) explore multiple schemes to estimate time-integrated spectra, while Ekanger et al. (2023) employs the neutrino spectrum calculated in 2D long-term simulations and updated star formation data.

In this study, we simply connected the CO core mass to the fate of the core collapse. However other parameters could be important to determine the ultimate fate (Pejcha & Thompson 2015; Ertl et al. 2016; Wang et al. 2022; Tsang et al. 2022; Takahashi et al. 2023). For improvements, systematic studies of core-collapse SNe could extend previous works in 1D simulations (O’Connor & Ott 2011; Ugliano et al. 2012; Sukhbold et al. 2016; Ebinger et al. 2020; Couch et al. 2020; Boccioli et al. 2021), 2D simulations (Nakamura et al. 2015; Summa et al. 2016; Vartanyan & Burrows 2023), and 3D simulations (Burrows et al. 2020). Simultaneously, more sophisticated input physics should be required, e.g., neutrino oscillation (Nagakura 2023; Ehring et al. 2023), neutrino reaction rate (Kotake et al. 2018; Sugiura et al. 2022), and equation of state (Fischer et al. 2014, 2020). Using such data, we can develop a better phenomenological treatment of the explosions (e.g., Belczynski et al. 2012).

There is much room for improvement in the assumptions used in this study. Even in the physics used in single star evolution we have uncertainties. For example, we have several recipes of wind mass loss rate (de Jager et al. 1988; Vink et al. 2000, 2001; Vink & de Koter 2005; Nugis & Lamers 2000), thereby impacting the core mass (e.g., Woosley et al. 2020). Advanced stages of stellar evolution lack strict

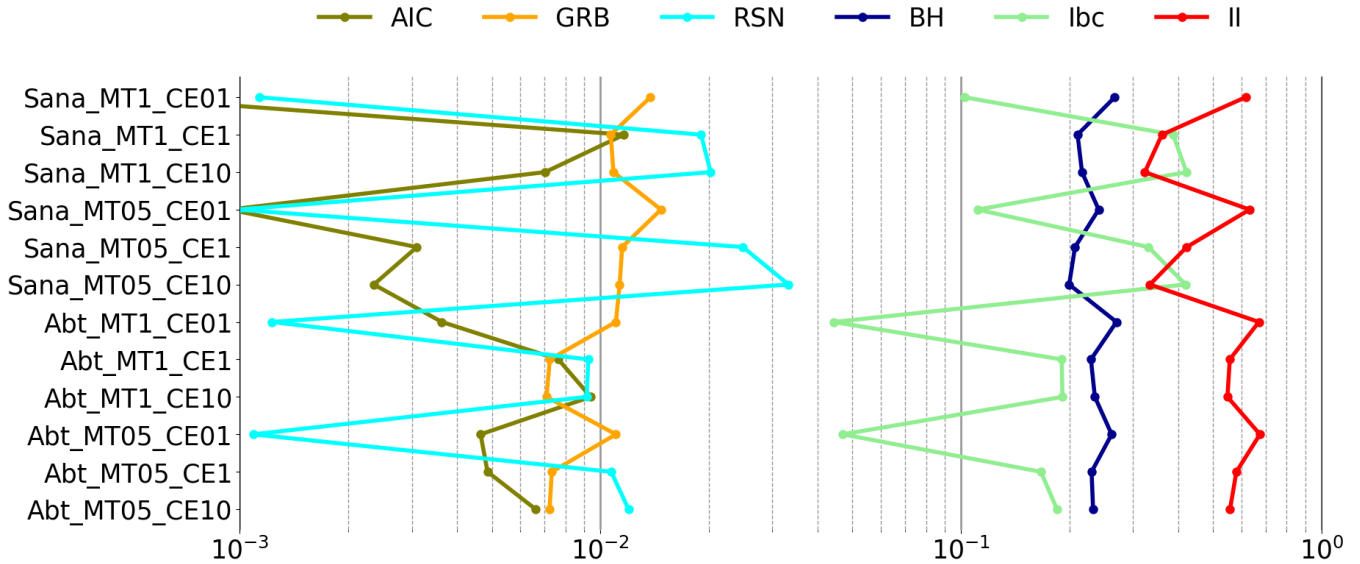


Figure 12. The fractions of each SN type for our 12 models, with binary fraction $f_b = 70\%$.

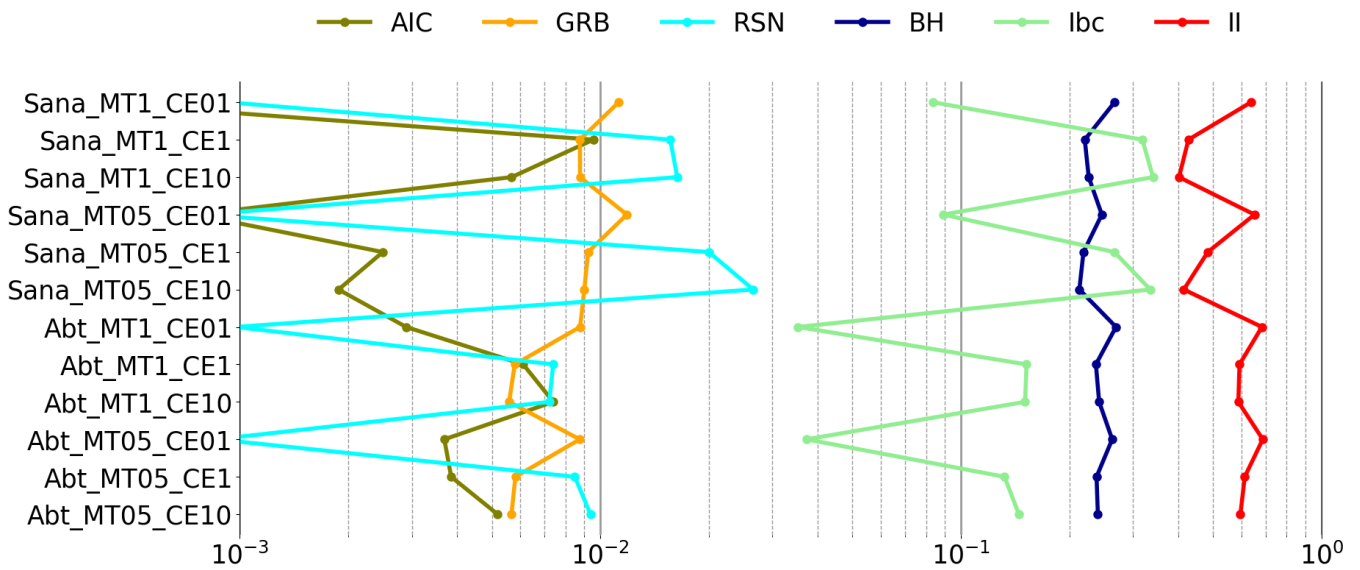


Figure 13. Same as Fig. 12 but with $f_b = 50\%$.

constraints on overshooting parameters (e.g., [Yoshida et al. 2019](#); [Temaj et al. 2023](#)) necessitating high-resolution simulations of convective shells for accurate determination ([Cristini et al. 2017](#)). We use REACLIB for the reaction rate of nucleosynthesis ([Cyburt et al. 2010](#)), but uncertainties with some reaction channels potentially alter stellar structures (e.g., [Takahashi et al. 2016](#)). The final stellar structure can also depend on numerical resolution (e.g., [Kato et al. 2020](#)). Angular momentum transport inside stars requires much theoretical efforts. The Tayler–Spruit dynamo is usually assumed (e.g., [Heger et al. 2005](#)) and wave-driven mechanism is also considered ([Fuller et al. 2015](#)). On binary star evolution, there are uncertainties about the mass transfer rate and the angular momentum loss ([Hirai 2023](#); [Willcox et al. 2023](#)). Despite these uncertainties, we have been able

to explore the progenitors behind major as well as rare SN types, and moreover their typical evolutionary paths. To make progress, it would be necessary to start from our study and systematically consider each uncertain factor, comparing and evaluating them in relation to observations one by one.

ACKNOWLEDGMENTS

We thank K. Takahashi, R. Hirai, and C. Lunardini for informative and stimulating discussions. This work was supported by the Research Institute of Stellar Explosive Phenomena at Fukuoka University and also by JSPS KAKENHI Grant Number (JP21K13915, JP21H01088, JP22H01223, JP22K03630,

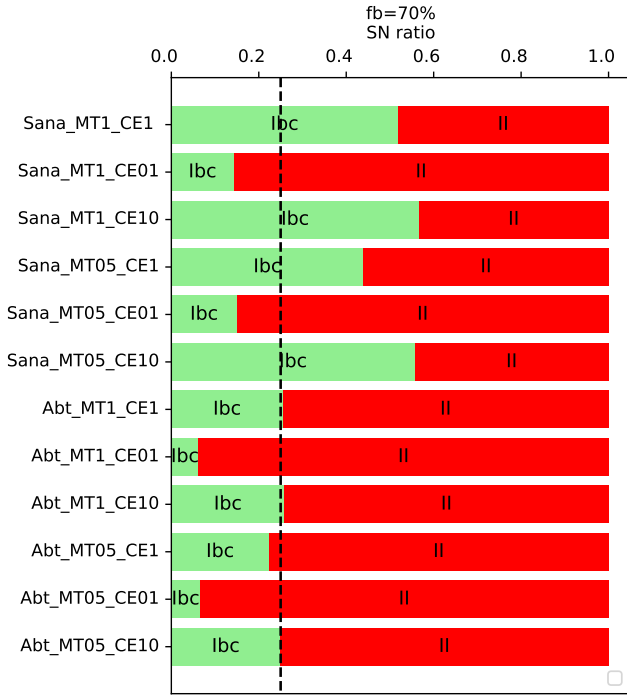


Figure 14. The ratio of Type II SNe to Type Ibc SNe for each binary synthesis model with binary fraction $f_b = 70\%$. The black dashed line is the SN ratio from observations (Li et al. 2011).

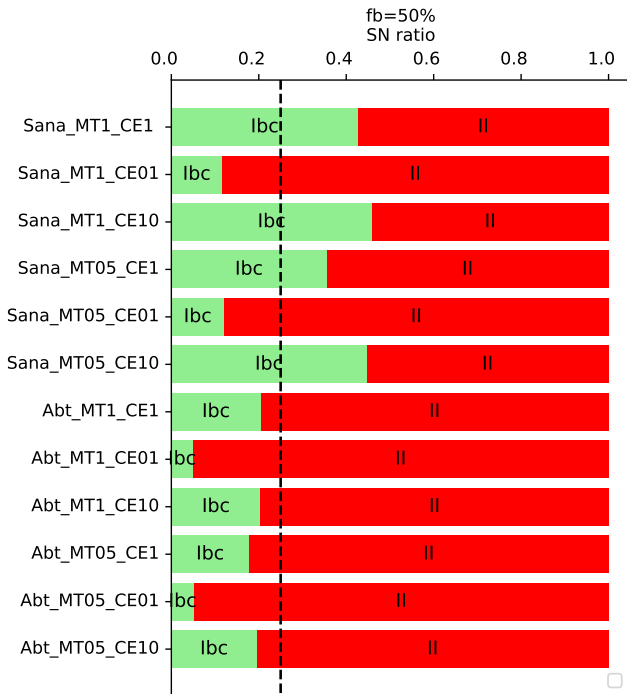


Figure 15. Same as Fig. 14 but for binary fraction $f_b = 50\%$.

JP23H04899, JP23H01199, and JP23K03400). The work of S.H. is also supported by the U.S. Department of Energy Office of Science under award number DE-SC0020262, and U.S. National Science Foundation Grant No. AST1908960 and No. PHY-2209420. This work was supported by World Premier International Research Center Initiative (WPI Initiative), MEXT, Japan. This research was also supported by MEXT as “Program for Promoting researches on the Supercomputer Fugaku” (Structure and Evolution of the Universe Unraveled by Fusion of Simulation and AI; Grant Number JPMXP1020230406) and JICFuS.

DATA AVAILABILITY

The data underlying this article will be shared on reasonable request to the corresponding author.

REFERENCES

- Abdikamalov E. B., Ott C. D., Rezzolla L., Dessart L., Dimmelmeier H., Marek A., Janka H. T., 2010, *Phys. Rev. D*, **81**, 044012
- Abe K., et al., 2021, *Phys. Rev. D*, **104**, 122002
- Abt H. A., 1983, *ARA&A*, **21**, 343
- Adams S. M., Kochanek C. S., Beacom J. F., Vagins M. R., Stanek K. Z., 2013, *ApJ*, **778**, 164
- Adams S. M., Kochanek C. S., Gerke J. R., Stanek K. Z., Dai X., 2017a, *Mon. Not. Roy. Astron. Soc.*, **468**, 4968
- Adams S. M., Kochanek C. S., Gerke J. R., Stanek K. Z., 2017b, *Mon. Not. Roy. Astron. Soc.*, **469**, 1445
- Aguilera-Dena D. R., Langer N., Moriya T. J., Schootemeijer A., 2018, *ApJ*, **858**, 115
- Ando S., Ekanger N., Horiuchi S., Koshio Y., 2023, in Proceedings of the Japan Academy, Series B. (arXiv:2306.16076)
- Ashida Y., Nakazato K., Tsujimoto T., 2023, *ApJ*, **953**, 151
- Basinger C. M., Kochanek C. S., Adams S. M., Dai X., Stanek K. Z., 2021, *Mon. Not. Roy. Astron. Soc.*, **508**, 1156
- Beacom J. F., 2010, *Annual Review of Nuclear and Particle Science*, **60**, 439
- Belczynski K., Kalogera V., Bulik T., 2002, *ApJ*, **572**, 407
- Belczynski K., Kalogera V., Rasio F. A., Taam R. E., Zezas A., Bulik T., Maccarone T. J., Ivanova N., 2008, *ApJS*, **174**, 223
- Belczynski K., Wiktorowicz G., Fryer C. L., Holz D. E., Kalogera V., 2012, *ApJ*, **757**, 91
- Boccioli L., Mathews G. J., O’Connor E. P., 2021, *ApJ*, **912**, 29
- Bollig R., Yadav N., Kresse D., Janka H.-T., Müller B., Heger A., 2021, *ApJ*, **915**, 28
- Breivik K., et al., 2020, *ApJ*, **898**, 71
- Bugli M., Guilet J., Foglizzo T., Obergaulinger M., 2023, *MNRAS*, **520**, 5622
- Burrows A., Radice D., Vartanyan D., Nagakura H., Skinner M. A., Dolence J. C., 2020, *MNRAS*, **491**, 2715
- Cantiello M., Yoon S. C., Langer N., Livio M., 2007, *A&A*, **465**, L29
- Chatzopoulos E., Frank J., Marcello D. C., Clayton G. C., 2020, *ApJ*, **896**, 50
- Chieffi A., Limongi M., 2020, *ApJ*, **890**, 43
- Chini R., Hoffmeister V. H., Nasserri A., Stahl O., Zinnecker H., 2012, *MNRAS*, **424**, 1925
- Cigan P., et al., 2019, *ApJ*, **886**, 51
- Conroy C., 2013, *ARA&A*, **51**, 393
- Couch S. M., Chatzopoulos E., Arnett W. D., Timmes F. X., 2015, *ApJ*, **808**, L21
- Couch S. M., Warren M. L., O’Connor E. P., 2020, *ApJ*, **890**, 127
- Cristini A., Meakin C., Hirschi R., Arnett D., Georgy C., Viallet M., Walkington I., 2017, *MNRAS*, **471**, 279
- Cyburrt R. H., et al., 2010, *ApJS*, **189**, 240
- De Marco O., Izzard R. G., 2017, *Publ. Astron. Soc. Australia*, **34**, e001
- Dominik M., Belczynski K., Fryer C., Holz D. E., Berti E., Bulik T., Mandel I., O’Shaughnessy R., 2013, *ApJ*, **779**, 72

- Ebinger K., Curtis S., Ghosh S., Fröhlich C., Hempel M., Perego A., Liebig M., Thielemann F.-K., 2020, *ApJ*, **888**, 91
- Eggleton P. P., 1983, *ApJ*, **268**, 368
- Eggleton P., 2011, *Evolutionary Processes in Binary and Multiple Stars*. Cambridge University Press
- Ehring J., Abbar S., Janka H.-T., Raffelt G., Tamborra I., 2023, *Phys. Rev. D*, **107**, 103034
- Ekanger N., Horiuchi S., Kotake K., Sumiyoshi K., 2022, *Phys. Rev. D*, **106**, 043026
- Ekanger N., Horiuchi S., Nagakura H., Reitz S., 2023, *arXiv e-prints*, p. [arXiv:2310.15254](https://arxiv.org/abs/2310.15254)
- Ekström S., et al., 2012, *A&A*, **537**, A146
- Eldridge J. J., Stanway E. R., 2022, *ARA&A*, **60**, 455
- Enoto T., Kisaka S., Shibata S., 2019, *Reports on Progress in Physics*, **82**, 106901
- Ertl T., Janka H. T., Woosley S. E., Sukhbold T., Ugliano M., 2016, *ApJ*, **818**, 124
- Fields C. E., 2022, *ApJ*, **924**, L15
- Fischer T., Hempel M., Sagert I., Suwa Y., Schaffner-Bielich J., 2014, *European Physical Journal A*, **50**, 46
- Fischer T., Wu M.-R., Wehmeyer B., Bastian N.-U. F., Martínez-Pinedo G., Thielemann F.-K., 2020, *ApJ*, **894**, 9
- Fragos T., et al., 2023, *ApJS*, **264**, 45
- Fryer C. L., Heger A., 2005, *ApJ*, **623**, 302
- Fryer C. L., Belczynski K., Wiktorowicz G., Dominik M., Kalogera V., Holz D. E., 2012, *ApJ*, **749**, 91
- Fujibayashi S., Sekiguchi Y., Shibata M., Wanajo S., 2023, *ApJ*, **956**, 100
- Fuller J., Cantiello M., LeCoanet D., Quataert E., 2015, *ApJ*, **810**, 101
- Gehrels N., Ramirez-Ruiz E., Fox D. B., 2009, *ARA&A*, **47**, 567
- Georgy C., Ekström S., Meynet G., Massey P., Levesque E. M., Hirschi R., Eggenberger P., Maeder A., 2012, *A&A*, **542**, A29
- Gerke J. R., Kochanek C. S., Stanek K. Z., 2015, *Mon. Not. Roy. Astron. Soc.*, **450**, 3289
- Giacobbo N., Mapelli M., Spera M., 2017, *Monthly Notices of the Royal Astronomical Society*, **474**, 2959
- Harada M., et al., 2023, *ApJ*, **951**, L27
- Heger A., Langer N., Woosley S. E., 2000, *ApJ*, **528**, 368
- Heger A., Fryer C. L., Woosley S. E., Langer N., Hartmann D. H., 2003, *ApJ*, **591**, 288
- Heger A., Woosley S. E., Spruit H. C., 2005, *ApJ*, **626**, 350
- Heggie D. C., 1975, *MNRAS*, **173**, 729
- Hijikawa K., Kinugawa T., Yoshida T., Umeda H., 2019, *ApJ*, **882**, 93
- Hirai R., 2023, *MNRAS*, **523**, 6011
- Hirai R., Sato T., Podsiadlowski P., Vigna-Gómez A., Mandel I., 2020, *MNRAS*, **499**, 1154
- Hjellming M. S., 1989, PhD thesis, Illinois Univ. at Urbana-Champaign, Savoy.
- Horiuchi S., Nakamura K., Takiwaki T., Kotake K., Tanaka M., 2014, *Mon. Not. Roy. Astron. Soc.*, **445**, L99
- Horiuchi S., Kinugawa T., Takiwaki T., Takahashi K., Kotake K., 2021, *Phys. Rev. D*, **103**, 043003
- Hsieh H.-F., Cabezon R., Ma L.-T., Pan K.-C., 2023, *arXiv e-prints*, p. [arXiv:2310.20411](https://arxiv.org/abs/2310.20411)
- Huang W., Gies D. R., McSwain M. V., 2010, *ApJ*, **722**, 605
- Hurley J. R., Pols O. R., Tout C. A., 2000, *MNRAS*, **315**, 543
- Hurley J. R., Tout C. A., Pols O. R., 2002, *MNRAS*, **329**, 897
- Hut P., 1981, *A&A*, **99**, 126
- Igoshev A. P., Frantsuzova A., Gourgouliatos K. N., Tsihli S., Konstantinou L., Popov S. B., 2022, *MNRAS*, **514**, 4606
- Ivanova N., Podsiadlowski P., Spruit H., 2002, *MNRAS*, **334**, 819
- Iwakami W., Nagakura H., Yamada S., 2014, *ApJ*, **793**, 5
- Janka H.-T., Wongwathanarat A., Kramer M., 2022, *ApJ*, **926**, 9
- Kato C., Hirai R., Nagakura H., 2020, *MNRAS*, **496**, 3961
- Keszthelyi Z., 2023, *Galaxies*, **11**, 40
- Kinugawa T., Asano K., 2017, *ApJ*, **849**, L29
- Kinugawa T., Inayoshi K., Hotokezaka K., Nakauchi D., Nakamura T., 2014, *MNRAS*, **442**, 2963
- Kinugawa T., Miyamoto A., Kanda N., Nakamura T., 2016, *MNRAS*, **456**, 1093
- Kinugawa T., Harikane Y., Asano K., 2019, *ApJ*, **878**, 128
- Kinugawa T., Nakamura T., Nakano H., 2020, *MNRAS*, **498**, 3946
- Kobulnicky H. A., Fryer C. L., 2007, *ApJ*, **670**, 747
- Kobulnicky H. A., et al., 2014, *ApJS*, **213**, 34
- Kochanek C. S., Beacom J. F., Kistler M. D., Prieto J. L., Stanek K. Z., Thompson T. A., Yuksel H., 2008, *Astrophys. J.*, **684**, 1336
- Kotake K., Takiwaki T., Fischer T., Nakamura K., Martínez-Pinedo G., 2018, *ApJ*, **853**, 170
- Kresse D., Ertl T., Janka H.-T., 2021, *ApJ*, **909**, 169
- Kuroda T., Arcones A., Takiwaki T., Kotake K., 2020, *ApJ*, **896**, 102
- Langer N., 2012, *ARA&A*, **50**, 107
- Laplace E., Justham S., Renzo M., Götborg Y., Farmer R., Vartanyan D., de Mink S. E., 2021, *A&A*, **656**, A58
- Larsson J., et al., 2023, *ApJ*, **949**, L27
- Li W., et al., 2011, *Monthly Notices of the Royal Astronomical Society*, **412**, 1441
- Liang E., Zhang B., Virgili F., Dai Z. G., 2007, *ApJ*, **662**, 1111
- Liang E.-W., Racusin J. L., Zhang B., Zhang B.-B., Burrows D. N., 2008, *ApJ*, **675**, 528
- Limongi M., 2017, *Supernovae from Massive Stars*. Springer International Publishing, p. 513, doi:10.1007/978-3-319-21846-5_119
- Longo Micchi L. F., Radice D., Chirenti C., 2023, *MNRAS*, **525**, 6359
- Lubow S. H., Shu F. H., 1975, *ApJ*, **198**, 383
- Lunardini C., 2016, *Astroparticle Physics*, **79**, 49
- Madau P., Dickinson M., 2014, *ARA&A*, **52**, 415
- Maeder A., 2009, *Physics, Formation and Evolution of Rotating Stars*. Springer, doi:10.1007/978-3-540-76949-1
- Mason B. D., Hartkopf W. I., Gies D. R., Henry T. J., Helsel J. W., 2009, *AJ*, **137**, 3358
- Matsumoto J., Asahina Y., Takiwaki T., Kotake K., Takahashi H. R., 2022, *MNRAS*, **516**, 1752
- McNeill L. O., Müller B., 2022, *MNRAS*, **509**, 818
- Menon A., Heger A., 2017, *MNRAS*, **469**, 4649
- Mocák M., Meakin C., Campbell S. W., Arnett W. D., 2018, *MNRAS*, **481**, 2918
- Moe M., Di Stefano R., 2017, *ApJS*, **230**, 15
- Mori M., Sawada R., Suwa Y., Tanikawa A., Kashiyama K., Murase K., 2023, *arXiv e-prints*, p. [arXiv:2306.17381](https://arxiv.org/abs/2306.17381)
- Müller B., Heger A., Liptai D., Cameron J. B., 2016a, *MNRAS*, **460**, 742
- Müller B., Viallet M., Heger A., Janka H.-T., 2016b, *ApJ*, **833**, 124
- Müller B., Gay D. W., Heger A., Tauris T. M., Sim S. A., 2018, *MNRAS*, **479**, 3675
- Nagakura H., 2023, *Phys. Rev. Lett.*, **130**, 211401
- Nakamura K., Takiwaki T., Kuroda T., Kotake K., 2015, *PASJ*, **67**, 107
- Nakamura K., Takiwaki T., Kotake K., 2022, *MNRAS*, **514**, 3941
- Neustadt J. M. M., Kochanek C. S., Stanek K. Z., Basinger C. M., Jayasinghe T., Garling C. T., Adams S. M., Gerke J., 2021, *Mon. Not. Roy. Astron. Soc.*, **508**, 516
- Nomoto K., Kobayashi C., Tominaga N., 2013, *ARA&A*, **51**, 457
- Noutsos A., Schnitzeler D. H. F. M., Keane E. F., Kramer M., Johnston S., 2013, *MNRAS*, **430**, 2281
- Nugis T., Lamers H. J. G. L. M., 2000, *A&A*, **360**, 227
- O'Connor E., Ott C. D., 2011, *ApJ*, **730**, 70
- Obergaulinger M., Aloy M. Á., 2020, *MNRAS*, **492**, 4613
- Obergaulinger M., Aloy M. Á., 2022, *MNRAS*, **512**, 2489
- Obergaulinger M., Janka H. T., Aloy M. A., 2014, *MNRAS*, **445**, 3169
- Ogata M., Okawa H., Fujisawa K., Yasutake N., Yamamoto Y., Yamada S., 2023, *MNRAS*, **521**, 2561
- Ono M., Nagataki S., Ferrand G., Takahashi K., Umeda H., Yoshida T., Orlando S., Miceli M., 2020, *ApJ*, **888**, 111
- Patton R. A., Sukhbold T., 2020, *MNRAS*, **499**, 2803
- Patton R. A., Sukhbold T., Eldridge J. J., 2022, *MNRAS*, **511**, 903
- Pejcha O., Thompson T. A., 2015, *ApJ*, **801**, 90
- Peters P. C., 1964, *Physical Review*, **136**, 1224
- Peters P. C., Mathews J., 1963, *Physical Review*, **131**, 435
- Pian E., et al., 2006, *Nature*, **442**, 1011

- Rasio F. A., Tout C. A., Lubow S. H., Livio M., 1996, *ApJ*, 470, 1187
- Riley J., et al., 2022, *ApJS*, 258, 34
- Salpeter E. E., 1955, *ApJ*, 121, 161
- Sana H., et al., 2012, *Science*, 337, 444
- Sana H., et al., 2013, *A&A*, 550, A107
- Schneider F. R. N., Podsiadlowski P., Müller B., 2021, *A&A*, 645, A5
- Sekiguchi Y., Shibata M., 2011, *ApJ*, 737, 6
- Shibagaki S., Kuroda T., Kotake K., Takiwaki T., 2020, *MNRAS*, 493, L138
- Shibagaki S., Kuroda T., Kotake K., Takiwaki T., Fischer T., 2023, *arXiv e-prints*, p. arXiv:2309.05161
- Smartt S. J., 2009, *ARA&A*, 47, 63
- Smith N., 2014, *ARA&A*, 52, 487
- Spera M., Mapelli M., Giacobbo N., Trani A. A., Bressan A., Costa G., 2019, *MNRAS*, 485, 889
- Stanway E. R., Eldridge J. J., 2018, *MNRAS*, 479, 75
- Sugiura K., Furusawa S., Sumiyoshi K., Yamada S., 2022, *Progress of Theoretical and Experimental Physics*, 2022, 113E01
- Sukhbold T., Ertl T., Woosley S. E., Brown J. M., Janka H. T., 2016, *ApJ*, 821, 38
- Sukhbold T., Woosley S. E., Heger A., 2018, *ApJ*, 860, 93
- Summa A., Hanke F., Janka H.-T., Melson T., Marek A., Müller B., 2016, *ApJ*, 825, 6
- Summa A., Janka H.-T., Melson T., Marek A., 2018, *ApJ*, 852, 28
- Taam R. E., Sandquist E. L., 2000, *ARA&A*, 38, 113
- Takahashi K., Langer N., 2021, *A&A*, 646, A19
- Takahashi K., Umeda H., Yoshida T., 2014, *ApJ*, 794, 40
- Takahashi K., Yoshida T., Umeda H., Sumiyoshi K., Yamada S., 2016, *MNRAS*, 456, 1320
- Takahashi K., Takiwaki T., Yoshida T., 2023, *ApJ*, 945, 19
- Takiwaki T., Kotake K., Foglizzo T., 2021, *MNRAS*, 508, 966
- Tanikawa A., Yoshida T., Kinugawa T., Takahashi K., Umeda H., 2020, *MNRAS*, 495, 4170
- Tauris T. M., et al., 2017, *The Astrophysical Journal*, 846, 170
- Temaj D., Schneider F. R. N., Laplace E., Wei D., Podsiadlowski P., 2023, *arXiv e-prints*, p. arXiv:2311.05701
- Tian Z.-J., et al., 2018, *Research in Astronomy and Astrophysics*, 18, 052
- Tsang B. T. H., Vartanyan D., Burrows A., 2022, *ApJ*, 937, L15
- Ugliano M., Janka H.-T., Marek A., Arcones A., 2012, *ApJ*, 757, 69
- Ulrich R. K., Burger H. L., 1976, *ApJ*, 206, 509
- Umeda H., Nomoto K., 2008, *ApJ*, 673, 1014
- Umeda H., Yoshida T., Takahashi K., 2012, *Progress of Theoretical and Experimental Physics*, 2012, 01A302
- Urushibata T., Takahashi K., Umeda H., Yoshida T., 2018, *MNRAS*, 473, L101
- Utrobín V. P., Wongwathanarat A., Janka H. T., Müller E., Ertl T., Menon A., Heger A., 2021, *ApJ*, 914, 4
- Varma V., Müller B., 2021, *MNRAS*, 504, 636
- Varma V., Müller B., Schneider F. R. N., 2023, *MNRAS*, 518, 3622
- Vartanyan D., Burrows A., 2023, *arXiv e-prints*, p. arXiv:2307.08735
- Vartanyan D., Laplace E., Renzo M., Götzberg Y., Burrows A., de Mink S. E., 2021, *ApJ*, 916, L5
- Vink J. S., de Koter A., 2005, *A&A*, 442, 587
- Vink J. S., de Koter A., Lamers H. J. G. L. M., 2000, *A&A*, 362, 295
- Vink J. S., de Koter A., Lamers H. J. G. L. M., 2001, *A&A*, 369, 574
- Wanderman D., Piran T., 2010, *MNRAS*, 406, 1944
- Wang T., Vartanyan D., Burrows A., Coleman M. S. B., 2022, *MNRAS*, 517, 543
- Webbink R. F., 1984, *ApJ*, 277, 355
- Willcox R., MacLeod M., Mandel I., Hirai R., 2023, *arXiv e-prints*, p. arXiv:2308.06666
- Wolff S. C., Strom S. E., Dror D., Lanz L., Venn K., 2006, *AJ*, 132, 749
- Woosley S. E., Bloom J. S., 2006, *ARA&A*, 44, 507
- Woosley S. E., Heger A., 2006, *ApJ*, 637, 914
- Woosley S. E., Heger A., 2007, *Phys. Rep.*, 442, 269
- Woosley S. E., Langer N., Weaver T. A., 1995, *ApJ*, 448, 315
- Woosley S. E., Heger A., Weaver T. A., 2002, *Reviews of Modern Physics*, 74, 1015
- Woosley S. E., Sukhbold T., Janka H. T., 2020, *ApJ*, 896, 56
- Wyder T. K., et al., 2005, *ApJ*, 619, L15
- Yadav N., Müller B., Janka H. T., Melson T., Heger A., 2020, *ApJ*, 890, 94
- Yoon S. C., Langer N., Norman C., 2006, *A&A*, 460, 199
- Yoshida T., Suwa Y., Umeda H., Shibata M., Takahashi K., 2017, *MNRAS*, 471, 4275
- Yoshida T., Takiwaki T., Kotake K., Takahashi K., Nakamura K., Umeda H., 2019, *ApJ*, 881, 16
- Yoshida T., Takiwaki T., Aguilera-Dena D. R., Kotake K., Takahashi K., Nakamura K., Umeda H., Langer N., 2021a, *MNRAS*, 506, L20
- Yoshida T., Takiwaki T., Kotake K., Takahashi K., Nakamura K., Umeda H., 2021b, *ApJ*, 908, 44
- Zahn J. P., 1975, *A&A*, 41, 329
- Zahn J. P., 1977, *A&A*, 500, 121
- Zapartas E., et al., 2017, *A&A*, 601, A29
- de Jager C., Nieuwenhuijzen H., van der Hucht K. A., 1988, *A&AS*, 72, 259

APPENDIX A: BINARY INTERACTIONS FOR SPIN AND ORBIT

A1 Tidal interaction

Tidal interaction changes the orbit and the spins of the binary system. There are two mechanisms for the dissipation of the tidal kinetic energy. One mechanism is the convective damping on the equilibrium tide for the stars with an outer convection envelope such as red giants. The other mechanism is the radiative damping on the dynamical tide for the stars with an outer radiative zone (Zahn 1977). The time evolution of the separation, the eccentricity, and the spin are calculated as

$$\frac{da}{dt} = -6 \frac{k}{T} q (1+q) \left(\frac{R_i}{a} \right)^8 \frac{a}{(1-e^2)^{\frac{15}{2}}} \times \left[f_1(e^2) - (1-e^2)^{\frac{3}{2}} f_2(e^2) \frac{\Omega_{\text{spin},i}}{\Omega_{\text{orb}}} \right], \quad (\text{A1})$$

$$\frac{de}{dt} = -27 \frac{k}{T} q (1+q) \left(\frac{R_i}{a} \right)^8 \frac{e}{(1-e^2)^{\frac{13}{2}}} \times \left[f_3(e^2) - \frac{11}{18} (1-e^2)^{\frac{3}{2}} f_4(e^2) \frac{\Omega_{\text{spin},i}}{\Omega_{\text{orb}}} \right], \quad (\text{A2})$$

$$\frac{d\Omega_{\text{spin},i}}{dt} = 3 \frac{k}{T} \frac{q^2}{r_g^2} \left(\frac{R_i}{a} \right)^6 \frac{\Omega_{\text{orb}}}{(1-e^2)^6} \times \left[f_2(e^2) - (1-e^2)^{\frac{3}{2}} f_5(e^2) \frac{\Omega_{\text{spin},i}}{\Omega_{\text{orb}}} \right], \quad (\text{A3})$$

where

$$f_1(e^2) = 1 + \frac{31}{2} e^2 + \frac{255}{8} e^4 + \frac{185}{16} e^6 + \frac{25}{64} e^8, \quad (\text{A4})$$

$$f_2(e^2) = 1 + \frac{15}{2} e^2 + \frac{45}{8} e^4 + \frac{5}{16} e^6, \quad (\text{A5})$$

$$f_3(e^2) = 1 + \frac{15}{4} e^2 + \frac{15}{8} e^4 + \frac{5}{64} e^6, \quad (\text{A6})$$

$$f_4(e^2) = 1 + \frac{3}{2} e^2 + \frac{1}{8} e^4, \quad (\text{A7})$$

$$f_5(e^2) = 1 + 3e^2 + \frac{3}{8} e^4. \quad (\text{A8})$$

where k/T , q , R_i , $\Omega_{\text{spin},i}$, Ω_{orb} , and r_g are the coupling parameter depending on the tidal interaction mechanism, the mass ratio, the radius of the star, the spin angular velocity of the star, the angular velocity of the orbit, and the dimensionless gyration radius of the star, respectively (Zahn 1977; Hut 1981). Notation i means 1 (primary star) or 2 (secondary star).

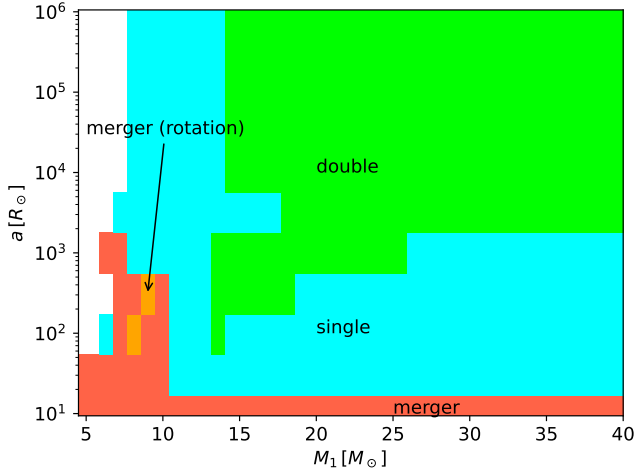


Figure A1. The binary progenitors of SNe in the $q = 0.5$ case.

If the star is a red giant, the convective damping of the equilibrium tide is effective. In this case, k/T is calculated as

$$\frac{k}{T} = \frac{2}{21} \frac{f_{\text{con}} M_{\text{env},i}}{\tau_{\text{con}} M_i}, \quad (\text{A9})$$

where $M_{\text{env},i}$, f_{con} , and τ_{con} are the stellar envelope mass, the correction factor of the tidal torque, and the eddy turnover timescale (e.g., Rasio et al. 1996; Hurley et al. 2002), respectively. They are calculated as

$$\tau_{\text{con}} = \left[\frac{M_{\text{env},i} R_{\text{env},i} \left(R_i - \frac{1}{2} R_{\text{env},i} \right)}{3L_i} \right]^{1/3}, \quad (\text{A10})$$

$$f_{\text{con}} = \min \left[1, \left(\frac{\pi |\Omega_{\text{orb}} - \Omega_{\text{spin},i}|^{-1}}{\tau_{\text{con}}} \right)^2 \right]. \quad (\text{A11})$$

where L_i and $R_{\text{env},i}$ are the stellar luminosity and the radius of the stellar envelope, respectively.

On the other hand, if the star have the radiative envelope i.e. the evolution stage is not a red giant, the tidal mechanism is the radiative damping of the dynamical tide (Zahn 1975). k/T is

$$\begin{aligned} \frac{k}{T} = & 4.3118 \times 10^{-8} \left(\frac{M_i}{M_{\odot}} \right) \left(\frac{R_i}{R_{\odot}} \right)^2 \\ & \times \left(\frac{a}{1 \text{ AU}} \right)^{-5} (1+q)^{5/6} E_2 \text{ yr}^{-1}, \end{aligned} \quad (\text{A12})$$

where E_2 is the tidal coefficient factor (Zahn 1977; Hurley et al. 2002).

A2 Magnetic braking

When a rotating star loses its mass, magnetic braking removes angular momentum from the rotating star via a magnetic field. The spin angular momentum loss by the magnetic braking is

$$\dot{J}_{\text{spin},i} = -5.83 \times 10^{-16} \frac{M_{\text{env},i}}{M_i} \left(R_i \Omega_{\text{spin},i} \right)^3 M_{\odot} R_{\odot}^2 \text{ yr}^{-2} \quad (\text{A13})$$

where masses and the radius are in solar units and Ω_{spin} in units of years (Hurley et al. 2000, 2002).

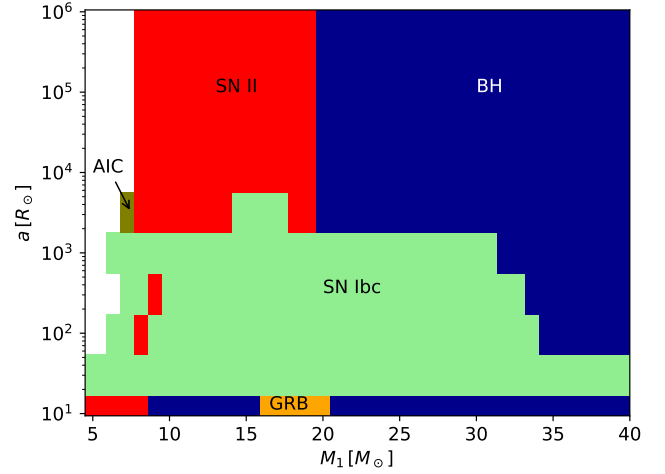


Figure A2. SN type of primary star in the $q = 0.5$ case.

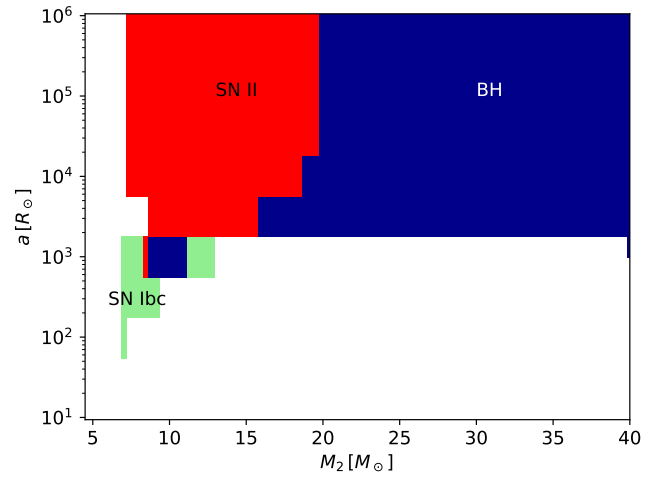


Figure A3. SN type of secondary star in the $q = 0.5$ case.

A3 Gravitational radiation

After the stars in a binary explode or collapse at the end of their lifetime, the compact star binary is formed. The compact binary loses the angular momentum and the orbital energy by the gravitational radiation. We use the weak-field approximation formalism given by Peters & Mathews (1963); Peters (1964). The loss of angular momentum, the orbital separation and the eccentricity are described as

$$\frac{\dot{J}}{J} = -\frac{32G^3 M_1 M_2 M_{\text{total}}}{5c^5 a^4} \frac{1 + \frac{7}{8} e^2}{(1 - e^2)^{5/2}}, \quad (\text{A14})$$

$$\frac{\dot{a}}{a} = -\frac{64G^3 M_1 M_2 M_{\text{total}}}{5c^5 a^4} \frac{1 + \frac{73}{24} e^2 + \frac{37}{96} e^4}{(1 - e^2)^{7/2}} \quad (\text{A15})$$

and

$$\frac{\dot{e}}{e} = -\frac{304G^3 M_1 M_2 M_{\text{total}}}{15c^5 a^4} \frac{1 + \frac{121}{304} e^2}{(1 - e^2)^{5/2}}. \quad (\text{A16})$$

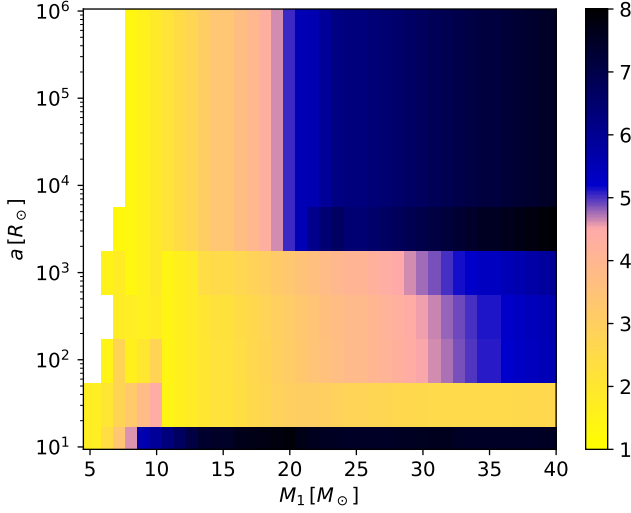


Figure B1. CO core mass of primary star in the $q = 0.5$ case.

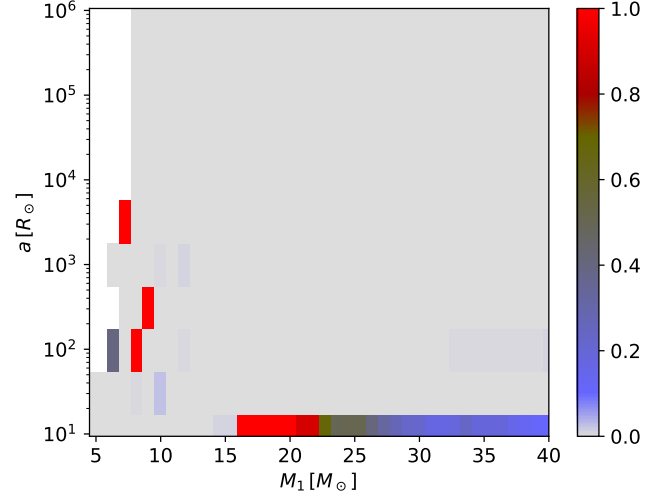


Figure B3. Angular momentum of primary star in the $q = 0.5$ case.

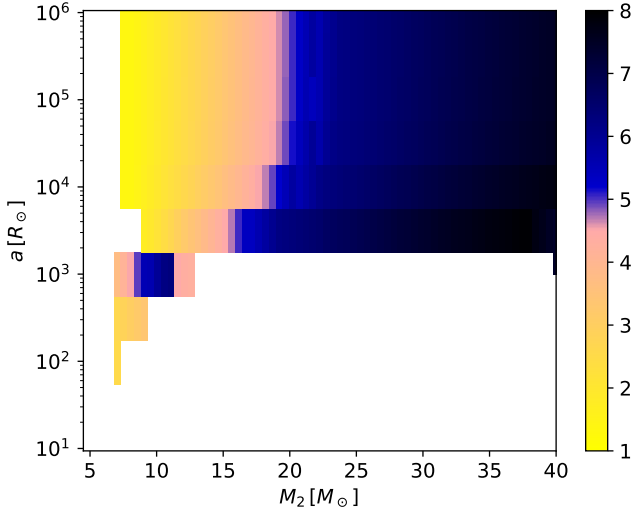


Figure B2. CO core mass of secondary star in the $q = 0.5$ case.

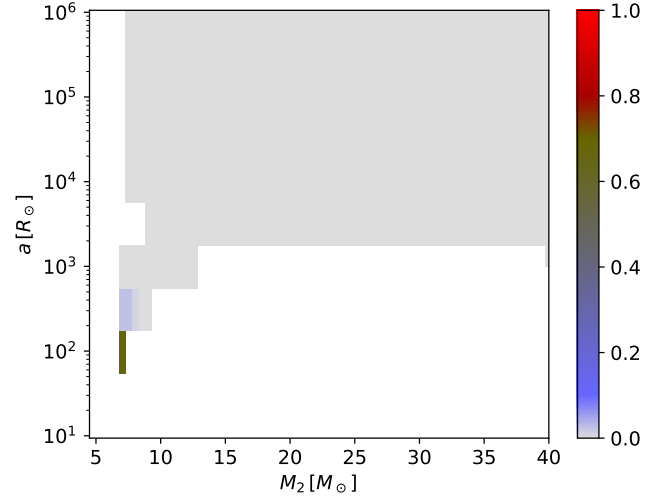


Figure B4. Angular momentum of secondary star in the $q = 0.5$ case.

APPENDIX B: PARAMETER SURVEY OF $Q=0.5$, AND 0.9 CASES

We show the parameter dependence of SN types, CO core mass, and angular momentum in the mass ratio of $q = 0.5$ and $q = 0.9$ while the case for $q = 0.7$ is discussed in Section 3.1.

B1 $q=0.5$ case

Figure A1 shows the progenitor of the SN in the mass ratio $q = 0.5$. Figures A2 and A3 show the fate of the primary star and the secondary star, respectively, as a function of their ZAMS mass and binary separation. Figures B1 and B2 show CO core mass as a function of their ZAMS mass and binary separation. Figures B3 and B4 show the angular momentum as a function of their ZAMS mass and binary separation.

The one of the main differences between this case and the $q =$

0.7 case is the absence of a pathway leading to RSN. See points $(M_1, a) = (8 M_\odot, 100 R_\odot)$, and $(9 M_\odot, 10^{2.5} R_\odot)$ in the Fig. A2, they collapse via merger (rotation). These progenitors evolve via a similar evolution path of RSN progenitor in the $q = 0.7$ case (left-hand side of Fig. 10). However, in these cases, the hydrogen envelopes remain and they collapse via type II SNe, although their CO cores have large angular momentum.

The other difference is that the type Ibc SNe occurs by secondary stars whose masses are $11 M_\odot \leq M_2 \leq 12.5 M_\odot$ with $a = 10^3 R_\odot$ (see Fig. A3). The SNe do not occur with the parameter range in $q = 0.7$ (see Fig. 3). BHs are formed from secondary stars whose masses are $9 M_\odot \leq M_2 \leq 11 M_\odot$ with $a = 10^3 R_\odot$ and that is similar to case of $q = 0.7$. When secondary masses are $9 M_\odot \leq M_2 \leq 11 M_\odot$ with $a = 10^3 R_\odot$, the secondary stars can become BHs due to the mass gain from the primary stars. However, when secondary masses are $11 M_\odot \leq M_2 \leq 12.5 M_\odot$ with $a = 10^3 R_\odot$, they get such a lot of masses from the primary stars that they become a common envelope and loses hydrogen envelopes. After the common envelope phase,

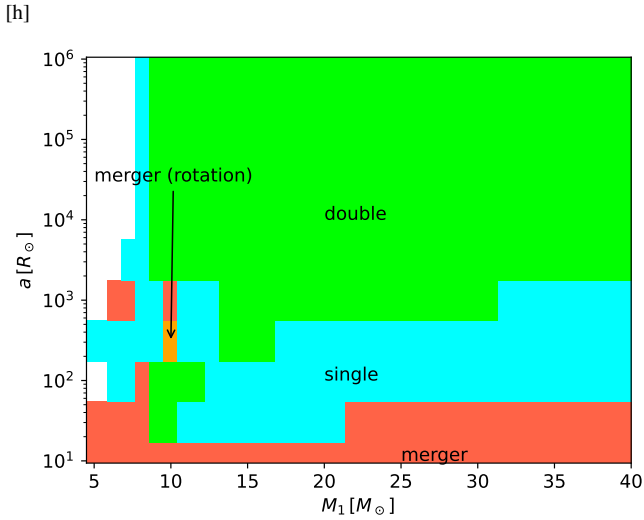


Figure B5. The binary progenitors of SNe in the $q = 0.9$ case.

the Wolf-Rayet stars lose a lot of masses due to the strong stellar wind mass loss and they cannot collapse to BHs.

B2 $q=0.9$ case.

Figure B5 shows the progenitor of the SN in the mass ratio $q = 0.9$. Figures B6 and B7 show the fate of the primary star and the secondary star, respectively, as a function of their ZAMS mass and binary separation. Figures B8 and B9 shows CO core mass as a function of their ZAMS mass and binary separation. Figures B10 and B11 show the angular momentum as a function of their ZAMS mass and binary separation.

The main differences of $q = 0.9$ case is another evolution path to RSN. The point of $(M_1, a) = (9 M_\odot, 10^{2.5} R_\odot)$ in Fig. B6 become RSN. Figure B12 shows the evolution path of this progenitor. The primary star loses the hydrogen envelope by the common envelope phase, but it can get enough mass and angular momentum by the mass transfer from the secondary star to occur a RSN. The secondary star, whose initial mass is enough massive to become a SN, cannot become a SN due to a lot of mass loss.

APPENDIX C: THE FRACTIONS OF EACH SN TYPE FOR 12 MODELS

In order to calculate the fractions of each SN type for 12 models We assume the binary fraction f_b as $f_b=70\%$ (e.g., Sana et al. 2012), and $f_b=50\%$ (e.g., Tian et al. 2018). According to Figure 2, in the case of effectively single stars, relatively light stars ($8 M_\odot < M < 20 M_\odot$) tend to become type II SN, while more massive ones ($> 20 M_\odot$) tend to become BH. If $f_b=70\%$, the number of type II SN and the number of BH increase 8163 and 2959, respectively. If $f_b=50\%$, the number of type II SN and the number of BH increase 19049 and 6903, respectively. We added these values to our result, in order to calculate the fractions of each SN type. Tables C1, and C2 show the fractions of each SN type for 12 models with $f_b = 70\%$, and $f_b = 50\%$, respectively.

This paper has been typeset from a \LaTeX file prepared by the author.

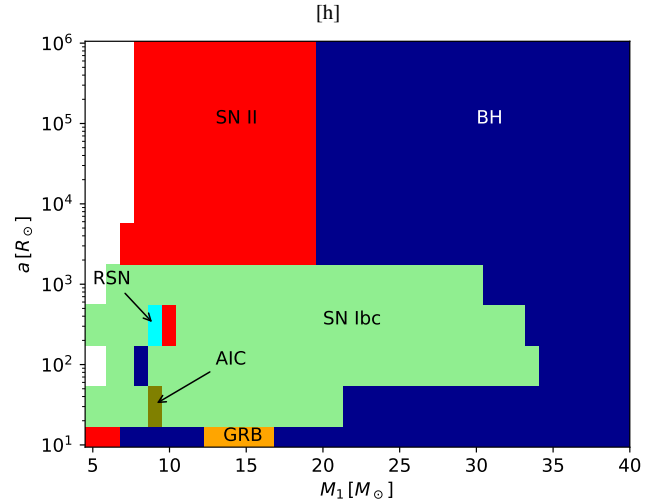


Figure B6. SN type of primary star in the $q = 0.9$ case.

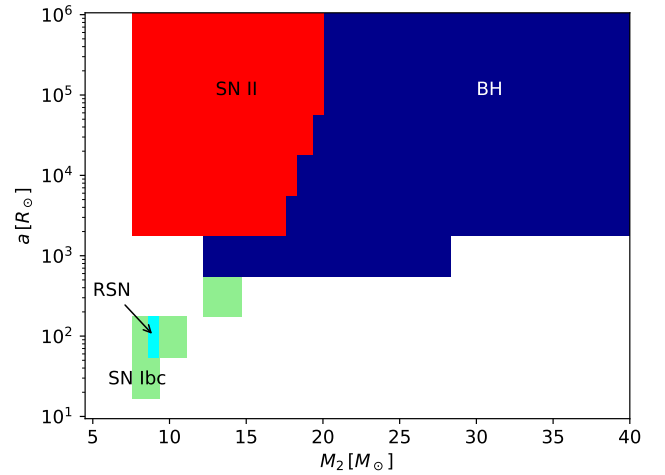


Figure B7. SN type of secondary star in the $q = 0.9$ case.

Table C1. The fractions of each SN type for 12 models with the binary fraction $f_b = 70\%$

model	AIC	Ibc	II	RSN	BH	GRB
Sana_MT1_CE01	0.000467628	0.102274784	0.615594642	0.001131358	0.266774271	0.013757316
Sana_MT1_CE1	0.011630121	0.387514464	0.360665583	0.019012465	0.210499334	0.010678033
Sana_MT1_CE10	0.007020693	0.421914822	0.323432766	0.020212544	0.216551525	0.010867649
Sana_MT05_CE01	0.000935377	0.111080114	0.631412255	0.000984607	0.240867767	0.014719879
Sana_MT05_CE1	0.003097751	0.330902118	0.422572609	0.024831181	0.207106799	0.011489543
Sana_MT05_CE10	0.002353262	0.419460455	0.334146175	0.033235565	0.199498653	0.01130589
Abt_MT1_CE01	0.003633029	0.044357559	0.669913326	0.00122831	0.269830286	0.011037489
Abt_MT1_CE1	0.007645104	0.190229184	0.556380526	0.009255492	0.229251424	0.00723827
Abt_MT1_CE10	0.009395388	0.191088011	0.548203609	0.00915914	0.235066422	0.00708743
Abt_MT05_CE01	0.004652061	0.047012148	0.674478618	0.001088407	0.261726705	0.011042062
Abt_MT05_CE1	0.004862751	0.166549209	0.580341097	0.010712146	0.230205434	0.007329363
Abt_MT05_CE10	0.00661415	0.184545927	0.557260702	0.011964923	0.232387039	0.007227259

Table C2. The fractions of each SN type for 12 models with $f_b = 50\%$

model	AIC	Ibc	II	RSN	BH	GRB
Sana_MT1_CE01	0.00038214	0.083577821	0.637250068	0.000924533	0.266623111	0.011242326
Sana_MT1_CE1	0.009554638	0.318359587	0.42729931	0.015619547	0.22039446	0.008772458
Sana_MT1_CE10	0.005672326	0.340883484	0.402294831	0.016330601	0.226038308	0.00878045
Sana_MT05_CE01	0.000752296	0.089338507	0.651501953	0.000791891	0.245776581	0.011838771
Sana_MT05_CE1	0.002492023	0.266198149	0.483478811	0.019975739	0.218612378	0.0092429
Sana_MT05_CE10	0.001878267	0.334794207	0.414865527	0.026527112	0.212911041	0.009023846
Abt_MT1_CE01	0.002891248	0.035300759	0.683009101	0.000977517	0.26903749	0.008783886
Abt_MT1_CE1	0.00610929	0.152014305	0.592072824	0.007396169	0.236623229	0.005784184
Abt_MT1_CE10	0.007400833	0.15052178	0.587657643	0.007214739	0.241622171	0.005582834
Abt_MT05_CE01	0.003691116	0.037301167	0.686784411	0.000863582	0.262598546	0.008761178
Abt_MT05_CE1	0.003855395	0.13204727	0.612183606	0.008493044	0.237609655	0.00581103
Abt_MT05_CE10	0.005185423	0.144682029	0.595449646	0.009380371	0.239636438	0.005666094

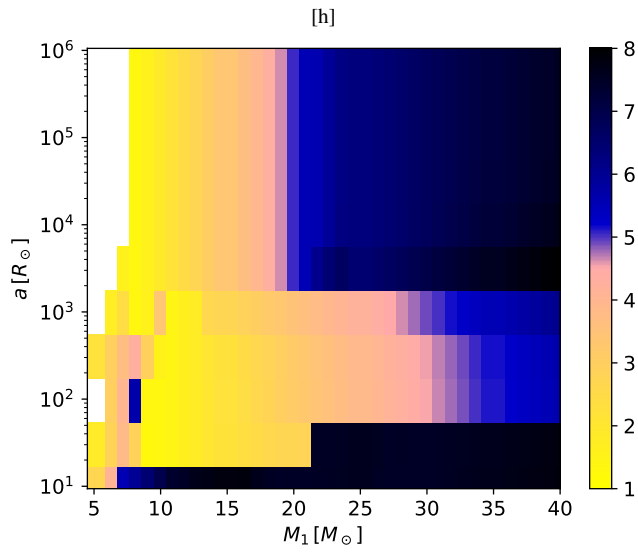


Figure B8. CO core mass of primary star in the $q = 0.9$ case.

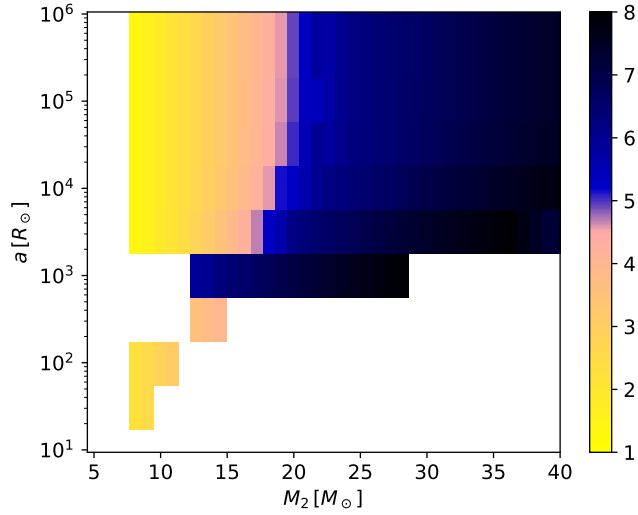


Figure B9. CO core mass of secondary star in the $q = 0.9$ case.

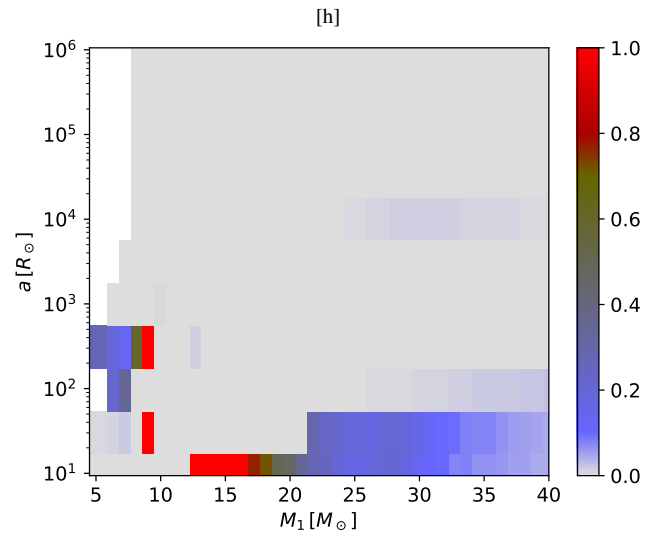


Figure B10. Angular momentum of primary star in the $q = 0.9$ case.

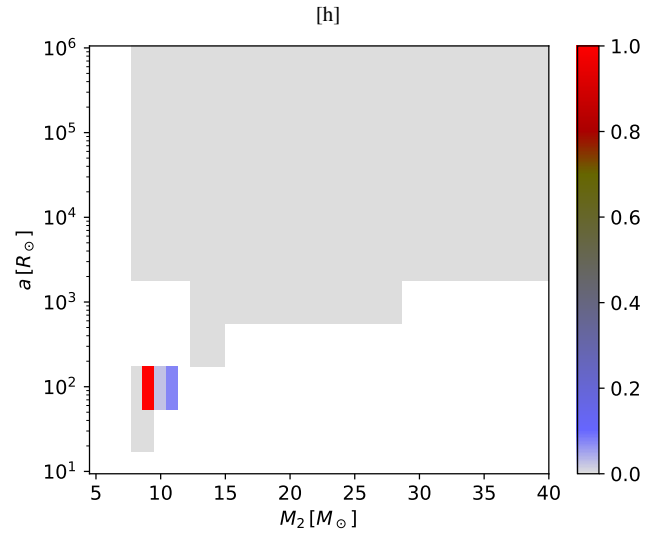


Figure B11. Angular momentum of secondary star in the $q = 0.9$ case.

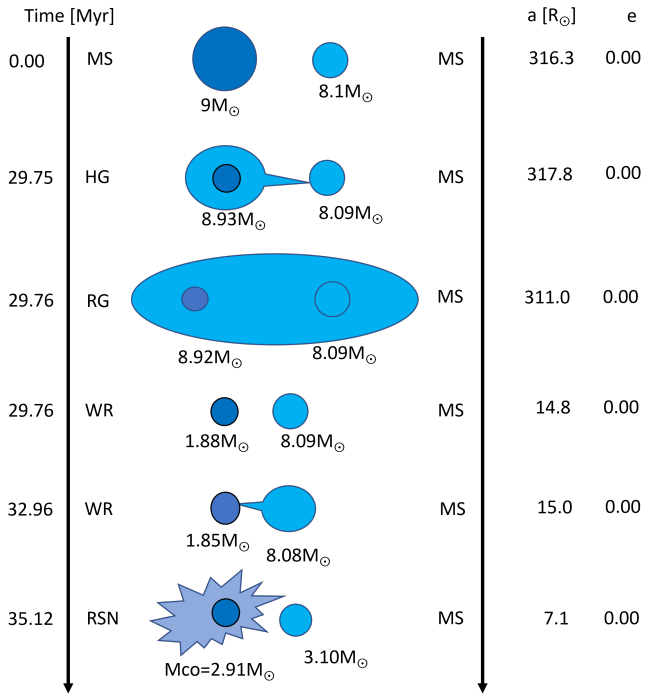


Figure B12. Example of the RSN progenitor evolutionary path in the case of $q = 0.9$. See Fig. 10 for other examples with $q = 0.7$.